Equatorward western boundary transport from the South Pacific: Glider observations, dynamics and consequences[☆,☆☆]

William S. Kessler[a,*], Hristina G. Hristova[a,b], Russ E. Davis[c]

[a] *NOAA/Pacific Marine Environmental Laboratory*
[b] *Joint Institute for Marine and Atmospheric Research, University of Hawai'i*
[c] *Scripps Institution of Oceanography*

Abstract

The Solomon Sea carries the equatorward western boundary current of the South Pacific, a principal element of subtropical-equatorial communication. Eighty-seven glider transects across the mouth of the Sea over nine years describe the velocity structure and variability of this system. The time series spans two El Niños and two La Niñas, which produced large transport anomalies, up to 50% of the mean. While transport increased during El Niños and decreased during La Niñas, their signatures were inconsistent among the events. Separated glider tracks show the merging of two inflows, one from the tropics east of the Solomon Island chain, the other entering as a western boundary current generated by winds over the full subtropical gyre. A model of linear wind-driven dynamics, including western boundary currents, had skill in describing the variability of the two inflows, identifying the distinct wind forcing driving each. The model suggests that both the mean and low-frequency variability of flow entering the Solomon Sea are driven remotely by wind over the South Pacific, acting through long Rossby waves. The ultimate significance of in situ observations in this

☆This is contribution number 4872 from the Pacific Marine Environmental Laboratory, and contribution number 18-396 from the Joint Institute for Marine and Atmospheric Research.

☆☆*Author contributions:* WSK: Original manuscript writing, data analysis, in situ data collection; HGH: data analysis and processing, editing, review, discussion; RED: experimental design and methodology, data analysis and processing, review, discussion.

Disclosure of interest: None

*Corresponding author: William S. Kessler, NOAA/Pacific Marine Environmental Laboratory, 7600 Sand Point Way NE, Seattle, WA 98115, USA; william.s.kessler@noaa.gov

small sea will be to describe its role in subtropical-tropical heat exchange that is crucial to ENSO and longer-timescale climate variations along the equator. We take an initial step here, suggesting that temperature advection through the Solomon Sea is a first-order contribution to interannual temperature changes of the equatorial strip as a whole.

Keywords: Tropical oceanography; Equatorial waves; Western boundary currents; Subtropical gyres; Wind-driven currents; Underwater vehicles; South Pacific Ocean; Solomon Sea

1. Introduction

Tsuchiya (1981) began modern interest in the Solomon Sea with his early demonstration that this small basin was the conduit for much of the flow from the South Pacific to the equator. Tsuchiya's schematic pathways, confirmed by more recent work (Toggweiler et al., 1991; Fine et al., 1994; Goodman et al., 2005; Pena et al., 2013), were based on sparse water property sampling. These measurements and Tsuchiya's interpretation gave impetus for the WEPOCS cruises of the late 1980s that added much local detail including early velocity moorings in the straits and a variety of biogeochemical measurements (Tsuchiya et al., 1989; Ganachaud et al., 2017). However, velocity sampling has remained limited and short-term (see Cravatte et al., 2011; Gasparin et al., 2012; Germineaud et al., 2016), despite the Solomon Sea's situation as a bottleneck where short coast to coast transport measurements provide a useful diagnostic of the subtropical-equatorial western boundary connection. Flow variations through the low-latitude western boundary currents of both hemispheres are known to be an important element of the recharge-discharge of mass and heat that is a crucial component of ENSO (Izumo et al., 2002; Kug et al., 2003; Lee and Fukumori, 2003; Izumo, 2005; Qin et al., 2015; Ishida et al., 2008), so reliable measurements of both quantities and their transport are required for both diagnosis and model development. The work described here is a response to this need, producing a 9-year (and ongoing) time series of temperature, salinity and velocity across the southern entrance to the Solomon Sea. It follows an earlier paper based on the first 3.5 years of the same glider transects (Davis et al., 2012).

This paper has three goals: To describe velocity, property and transport patterns in the Solomon Sea as seen by 33 glider missions spanning 2007–2016, including the sources of error and uncertainty in this sampling (sections 2–4); to assess the mechanisms driving this variability and its structure on annual and interannual timescales using a simple wind-driven model of the South Pacific (section 5); and to use the glider velocity and temperature measurements in a preliminary evaluation of the impact of Solomon Sea temperature advection on the basinwide equatorial strip (section 6).

Two crucial features of the South Pacific determine overall Solomon Sea velocity structure. First, the roughly 15 Sv transport of the Indonesian Throughflow (ITF; Sprintall et al., 2009) makes the Solomon Sea fundamentally different from other western boundary current (WBC) systems. Unlike most other such systems that primarily balance Sverdrup transport integrated over the gyres to their east, Solomon Sea mean flow is dominated by the net northward transport through the South Pacific required by the ITF.

Consider the situation in the South Pacific with the ITF either open or closed, keeping identical winds in each case, and ignoring Bering Strait. If the ITF were closed, total mean meridional transport between South America and Australia/New Guinea would be zero (as it is across the North Pacific). Both the strong subtropical anticyclonic and weaker tropical cyclonic gyres would be completed by WBCs that balanced Sverdrup transport at each latitude, thus strongly southward along the coast of central Australia and weakly northward in the Solomon Sea. With the ITF open, an additional northward transport of about 15 Sv is required at all latitudes from Tasmania to the equator. Given identical winds, the interior Sverdrup gyres would be identical in both cases, so in a linear, vertically-integrated sense the transport difference could only occur in the WBCs. The actual situation is certainly more complex than this, as the heat drained by the ITF from the Pacific to the Indian Ocean (Lee et al., 2002) likely induces a complex set of coupled basin-scale modifications to the entire gyres, but the first-order deduction is that a principal effect of the ITF is to add about 15 Sv northward transport to both South Pacific WBCs. Instead of strong subtropical and weak tropical WBCs, the open ITF reverses their magnitudes to suggest a very strong tropical and relatively weak subtropical WBC. This topic is discussed further in section 5.

The second key dynamical feature of the South Pacific affecting the Solomon Sea is its thick subtropical gyre, with outcropping isopycnals to at least sigma 27.2, which feeds the subthermocline WBC (section 4; Tsuchiya, 1981; Kessler and Cravatte, 2013b). The roughly 15 Sv required by the Indonesian Throughflow appears to enter lower thermocline layers of the gyre from the southeastern Pacific at isopycnals near sigma 27 or deeper (Iudicone et al., 2007). Subduction of this water occurs at the Subantarctic Front, whose position is furthest south in the eastern Pacific and lends higher densities to these water masses than is typical of this front in other basins (McCartney, 1982), ventilating this relatively deep subthermocline layer and eventually flowing in the lower gyre to the low-latitude WBC. Yet-unknown processes occurring in unknown locations as this water circulates around both the North and South Pacific must produce its modification either in the Solomon Sea (Alberty et al., 2017) or after transiting the Solomon Sea, because water leaves the Pacific in the ITF at much lower densities. By contrast, the corresponding equatorward WBC in the North Pacific (the Mindanao Current) is much shallower, with both its mean and variability surface-intensified and occurring mostly above 300 m (Schonau and Rudnick, 2017).

Beyond these defining mean features, Solomon Sea variability plays a large role in interannual fluctuations of Pacific tropics because water flowing through the Sea is a principal source for the equatorial current system (Scully-Power, 1973; Tsuchiya, 1981; Tsuchiya et al., 1989; Davis, 2005; Grenier et al., 2011), so changes in the either the mass transport or properties of that transport (set where the water is subducted into the subtropical gyre) can potentially affect the evolution on the equator. We will show that Solomon Sea transport is strongly correlated with ENSO variability (section 4), and further, that temperature advection through the Solomon Sea is a large influence on interannual heat content variability over the entire equatorial band (section 6).

2. Data and processing

2.1. Glider sampling

Thirty-seven gliders have been launched in the Solomon Sea, with the first in July 2007 and the latest mission used here in August 2016. Three of these failed before completing any coast-to-coast transects, two due to apparent fish strikes, one to internal component problems; all were recovered. Three more deployments failed after completing at least one transect and were also recovered; no gliders have been lost during this period. One other mission was used to explore the northern Solomon Sea and is not discussed here. The 33 partly or completely successful missions, with almost 17,000 individual dives covering more than 70,000 km, accomplished 87 coast-to-coast transects (Fig. 1). However, the failures, as well as shipping and other operational delays, introduced a few long gaps in the time series; the longest of these was 193 days in early 2009, with two successive gaps of more than 100 days in 2010 (ticks on the time axis of Fig. 2). Consequences of these gaps for the interpretation are discussed in section 2.2 below.

Here, “coast-to-coast” means gliders approach within 5 km of the shallow reefs at each end of the transect. This close approach is particularly important on the western (New Guinea) side where the flow is strong close to the coast. After some early experimentation, our western endpoint was chosen as Rossel Island at the eastern end of the Louisiade Archipelago that extends from the mainland of Papua New Guinea (Fig. 1). Channels between islands in this chain are shallow (less than 250 m deep) and/or narrow (less than 10 km wide), so Rossel Island appears to be a reliable endpoint.

Similarly, the islands of the Solomons chain are separated by shallow and narrow channels from the southern tip of Guadalcanal at 10°S to Buka Island at

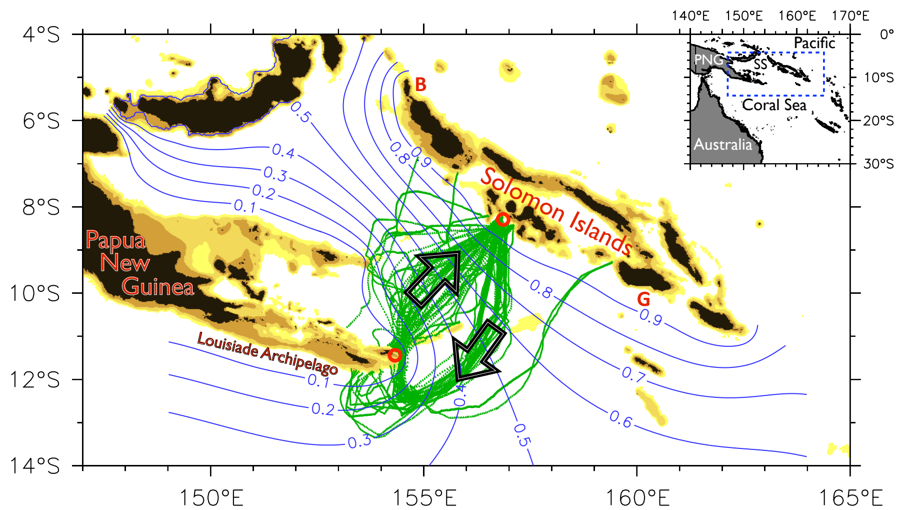

Figure 1: Bathymetric map of the Solomon Sea (brown shading, with levels 100 m, 500 m and 1000 m). Green dots show the approximately 17,000 glider dives and their separated southern (westbound) and northern (eastbound) tracks, with arrows showing the track direction. Red circles show the endpoints of the glider transects; the launch point (Gizo) at northeast, and turnaround point (Rossel) at southwest. Labels "G" and "B" show the locations of Guadalcanal and Buka Islands, respectively, the limits of the nearly-continuous part of the Solomon Island chain. Blue contours show the coordinate ϕ used to associate data from the irregular tracks (section 2.3). The small inset map situates the Solomon Sea in the southwest Pacific.

5°S (Fig. 1), forming an essentially solid barrier to large-scale ocean circulation. In the east, we launch and recover gliders out of Gizo, Solomon Islands, the nearest point opposite Rossel that has shipping and air service. The Gizo-Rossel transect thus measures virtually all flow entering the Solomon Sea from the South Pacific. Currents are generally much weaker in the east, and Gizo is in a broad indentation of the coast with consistently weak currents. We also launched two early missions out of Honiara while learning to work in this remote country.

The Spray glider makes 20–25 cm s^{-1} through the water (Rudnick and Cole, 2011). Since Solomon Sea currents can be as large or larger than this, we cannot accomplish straight-line transects across the Sea, especially in the verticallythick, fast WBC. Instead, westbound gliders (outbound from Gizo) must track south and offshore of the boundary current, returning on a shorter transect about 200 km to the north, yielding a clockwise route (Fig. 1). The tracks thus naturally produce two separated transects which have distinct velocity characteristics, discussed in section 4 below.

For the first 6 years of the project, early-generation Spray gliders were capable of a single round-trip across the Sea, and required project personnel to be present at each deployment and recovery; these two factors limited our sampling which averaged 58 days between transects. This was barely adequate to resolve the signals of interest (section 3), and was subject to longer gaps if something went wrong as noted above. Since mid-2013, technical improvements to the gliders have allowed them to go deeper and faster, producing two round-trips per mission. In addition, we have trained Solomon Islanders to deploy and recover gliders we build and store there, allowing better spacing of missions. These two improvements have reduced the average time between transects to 26 days (ticks along the bottom of Fig. 2).

The improved gliders also allowed the dive depths to increase during the project. Of the 87 transects discussed here, the first sampled to 500 m, the next four to 600 m, the next 30 to 700 m, and the last 52 to 1000 m.

Spray gliders measure temperature and salinity using a Seabird 41-CP pumped CTD. They infer vertical-mean absolute velocity, averaged over the 4–5 hours of a dive, from the observed dive and resurface positions and a flight model that estimates the glider's motion relative to the water velocity based on the known three-dimensional orientation of the glider throughout its dive (Sherman et al., 2001; Davis et al., 2012; Rudnick and Cole, 2011; Rudnick et al., 2016). Quality-controlled temperature and salinity profiles and vertical-mean horizontal velocities for the 33 missions considered here are available at `https://spraydata.ucsd.edu/projects/Solomon` (Davis, 2016). Additional corrections are applied to the vertical-mean velocities to account for effects of fouling and sideslip as described in Davis et al. (2012) (Appendix). These produce an RMS difference of 2 Sv from the standard flight model that uses a default angle

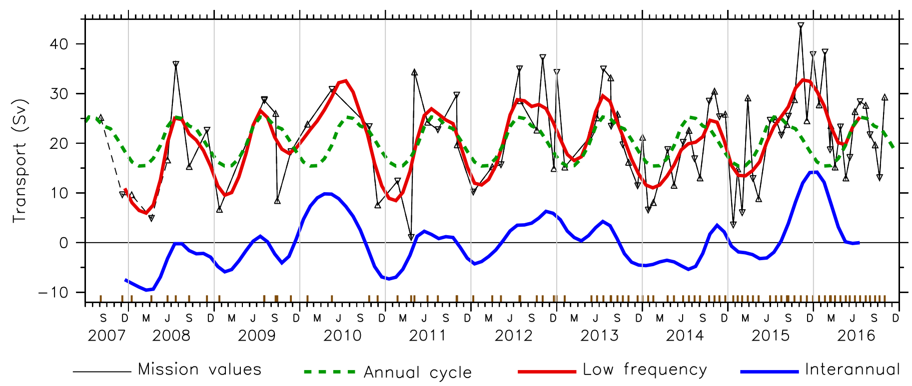

Figure 2: Time series of coast-to-coast equatorward transport above 700 m (Sv). Black line with triangles shows the 87 transect values; upward-pointing triangles show eastbound transects, downward-pointing westbound, and brown ticks at bottom show the central date of each transect. The first 5 transects are connected by dashed lines to indicate that they result from a downward extrapolation (section 2.2). As indicated in the legend, the green dashed line shows the average annual cycle of these, the blue line shows the interannual anomalies (see section 2.1), and the red line shows the "low-frequency" time series, which is the sum of the annual cycle plus the interannual anomalies.

of attack; the difference is smaller than the typical geophysical errors caused by slow sampling in a field of vigorous eddies (section 3). Prior to computing crosstrack geostrophic shear, we remove high frequency variability from the data by an along-track objective mapping using a Gaussian covariance matrix with a 3.5 days decorrelation scale and noise-to-signal ratio of 0.01.

2.2. Glider transport estimation

The combination of absolute vertically-averaged velocity with geostrophic crosstrack shear derived from the observed density yields the absolute geostrophic crosstrack velocity v_N as a function of depth and glider position. Ekman transport is at least an order of magnitude smaller, with its importance reduced here because winds (and their annual cycle variability) in the Solomon Sea tend to be along the axis of the Sea (Fig. 3a), so the resulting cross-Sea Ekman contribution makes a small contribution to the equatorward transport of interest here.

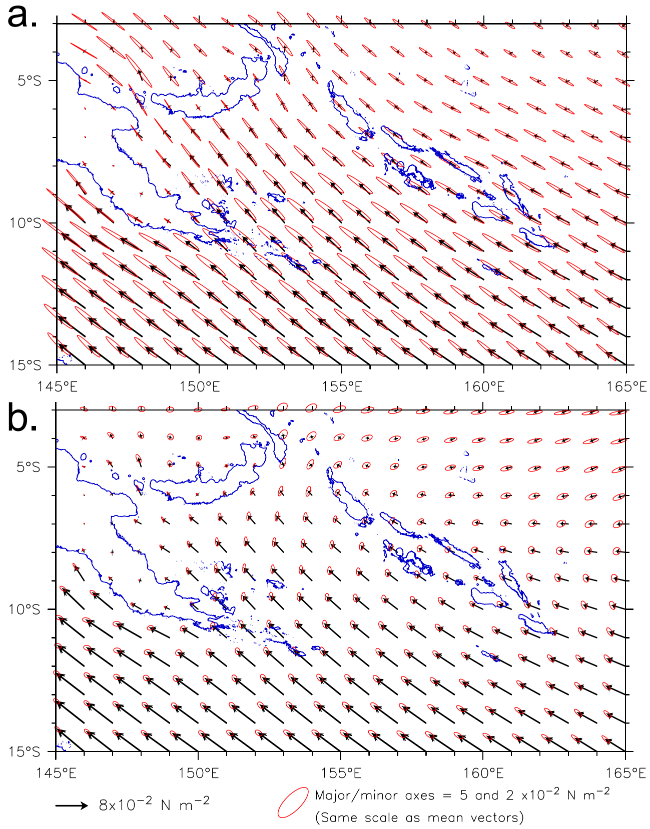

Figure 3: Wind stress variance ellipses for (a) annual cycle and (b) interannual anomalies. Black vectors are means. Both panels use the same scale for vectors (lower left) and ellipses (lower right).

Coast to coast volume transport Q ($\mathrm{m}^3\ \mathrm{s}^{-1}$) is

$$Q(t) = \int_{-D}^{0} \int_{0}^{L} v_N(s, z)\, ds dz \tag{1}$$

where v_N is the absolute geostrophic crosstrack current, ds is the alongtrack distance of each glider dive with L the total transect length, and z is depth with D the total dive depth. Q is the quantity shown in Figs. 2 and 4, and wherever glider-measured transport is compared with other measures (e.g., Fig. 10 and the top panels of Figs. 15 and 16).

Since much of the transport variability is shallow, we considered reporting transport values only over the deepest common depth of 500 m, which would omit a large fraction of the data. Experience with the deeper missions shows that the coast-to-coast transport integral (though not the dive-by-dive velocity itself) has a consistent linear vertical shear between 400 and 700 m, with correlations above 0.98 for these depth ranges. We thus use a linear least squares fit to extrapolate the five early shallow transport integrals to 700 m; transport time series discussed here include this extrapolation (Fig. 2). However, although more than half the transects extended to 1000 m, these coincided with the recent frequent repeats, covering only about the last one-third of the time series length; we therefore did not consider this adequate to extrapolate the early transects to 1000 m.

The few long gaps posed a second difficulty in estimating a consistent time series. As mentioned above, the year 2010 was poorly sampled with only 4 transects, in January, May, October and November (ticks on the time axis of Figs. 2 and 4). That year saw the termination of one of the two El Niños during this period (maximum Niño3.4 SST in Dec 2009) and the subsequent large transport decrease due to La Niña (minimum in Nov 2010). Apparently-large fluctuations of Solomon Sea transport occurred during 2010, including an equatorward transport peak that is one of the larger events in our record. As we are interested in the low-frequency transport variations, and have no expectation that the present sampling could resolve frequencies higher than seasonal (section 3), we used the following procedure to estimate a low-frequency time series of transport:

1. Piecewise-linearly interpolate the irregularly-spaced transport values to daily, then smooth with a 3-month running mean applied twice (5-month triangle filter);
2. Compute an average annual cycle by taking 12 monthly averages;
3. Interpolate this annual cycle to the original transect dates, subtract it from each mission's transport value;
4. Define the interannual anomaly as the difference in step 3, and smooth

again with a 3-month running mean applied twice.

Three time series result from this procedure: the average annual cycle from step 2 (green dashes in Fig. 2), the interannual anomaly from step 4 (blue line in Fig. 2, and Fig. 4), and the "low-frequency transport time series" defined as the sum of these two (red line in Fig. 2). Although the linear interpolation in step 1 is a strong assumption where the sampling is sparse, as it was in 2009 and 2010, we have no confidence that any method would produce a more credible estimate, and therefore chose the simplest.

2.3. Irregular glider tracks and their complications

Because the glider speed through the water is similar to that of the currents it encounters, the pathways taken during transects are not uniform (Fig. 1). With complicated coastlines, varying width of the Sea, and narrow currents strongly tied to the New Guinea side, it is not straightforward to construct averages or low-pass filters when, for example, the glider crosses the western boundary current at varying locations.

As the important coordinate is distance from the coast of New Guinea, we introduce a cross-basin coordinate $\phi(x, y)$, defined by $\nabla^2\phi = 0$, and made to follow coastlines by boundary conditions $\phi = 0$ on the New Guinea coast, and $\phi = 1$ on the Solomons coast (Fig. 1). Manual adjustments were made in a

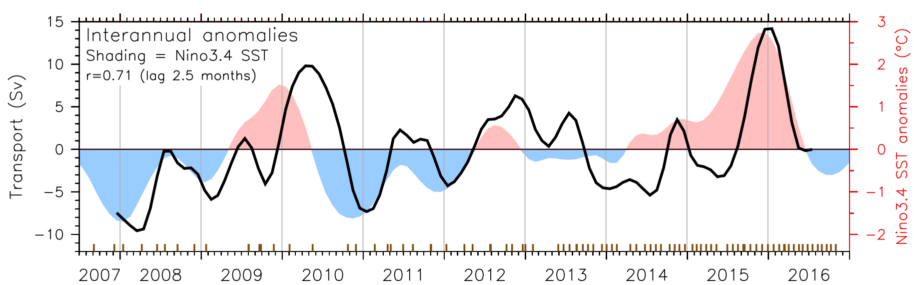

Figure 4: Interannual anomalies of glider-measured equatorward transport (black line; Sv) overlaid on anomalies of Niño3.4 SST (color shading, scale at right, where pink indicates El Niño and blue La Niña tendencies).

few places to avoid small islands and narrow bays. These choices define ϕ with a smooth gradient across the Solomon Sea, and its contours approximate the generally equatorward flow paths observed (Davis et al., 2012).

For scalars like temperature and salinity, ϕ is simply a cross-basin coordinate that allows averaging, providing a reference to compare values at different latitude-longitude values but similar locations relative to the basin width. Describing velocity is more complex. Although the gliders measure both components of depth-averaged velocity, only the crosstrack component of shear is known. While crosstrack current v_N defines transport unambiguously when integrated coast to coast, individual samples of v_N can be a poor velocity descriptor because they depend both on the direction of glider track to which v_N is normal, and on the ocean currents it measures. More useful descriptors are obtained by writing the coast-to-coast transport (1) in terms of ϕ, or in terms of its perpendicular r, the distance across the basin moving normal to ϕ (see Fig. 5):

$$
\begin{aligned}
Q(t) &= \int_{-D}^{0}\int_{0}^{1} \frac{ds}{d\phi} v_N(s,z)\, d\phi dz \\
&= \int_{-D}^{0}\int_{0}^{R} \frac{ds}{dr} v_N(s,z)\, dr dz
\end{aligned}
\tag{2}
$$

The glider's alongtrack progress Δs, its position $\phi_g(x,y,t)$ and progress across ϕ-contours $\Delta\phi$, and the perpendicular distance Δr between ϕ-contours at $\phi_g(x,y,t)$ are straightforwardly found from the sequence of glider dives. The integrand of the second of (2) defines the useful quantity u_ϕ:

$$
u_\phi \equiv \frac{ds}{dr} v_N(s,z)
$$

which thus represents cross-track velocity (m s^{-1}) projected on ϕ-contours, with the positive direction chosen equatorward (Fig. 5). We refer to u_ϕ as a pseudo-velocity, not a physical quantity; it is the velocity that when integrated in Δr would produce the measured transport Q, hence an appropriate way to compare or average measured v_N on tracks in different locations. While u_ϕ is thus useful to display equatorward velocity in familiar units, it is most suitable when the

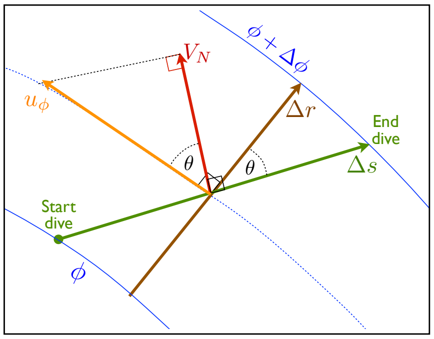

Figure 5: Schematic diagram showing the relations among the vectors Δs (glider motion during a single dive from ϕ to $\phi + \Delta\phi$), Δr (perpendicular to ϕ contours, with angle θ from Δs), V_N (crosstrack transport, perpendicular to Δs), and the pseudo-velocity u_ϕ (parallel to ϕ contours; section 2.3).

glider path is nearly perpendicular to contours of ϕ, so that the cross-track velocity v_N we measure is largely the same as u_ϕ (Fig. 5). Conversely, when the glider path Δs is nearly parallel to contours of ϕ, the usefulness of cross-track shear to describe equatorward, along-ϕ flow is degraded, and the effect of small errors becomes magnified. For this reason, we restrict the calculation of u_ϕ to where the angle θ between the track direction Δs and the perpendicular to ϕ contours Δr is less than 70° (Fig. 5). Overall about 92% of dives met this standard, though it is inevitably common that gliders tend to follow ϕ contours near the west endpoint of our transects while being swept downstream in the strong current near the coast; the majority of the glider dives that could not be used to calculate u_ϕ are west of $\phi = 0.3$. Thus, although u_ϕ formally produces an identical transport Q when integrated coast to coast as in (2), u_ϕ is used here only as a convenient way to display velocity on cross-Sea transects (e.g., Fig. 6). Transport calculations reported here are found unambiguously by integrating v_N coast to coast (equation (1)).

2.4. Wind data (CCMP v2.0)

The Cross-Calibrated Multi-Platform (CCMP) version 2 product combines Version-7 RSS radiometer wind speeds, QuikSCAT and ASCAT scatterometer

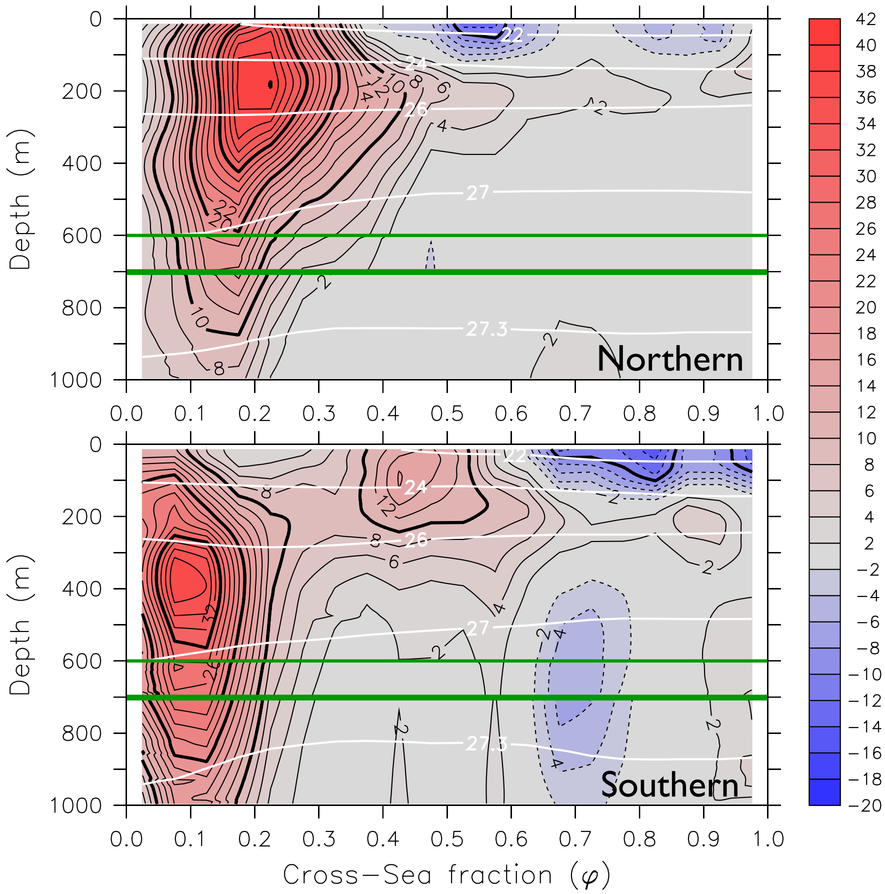

Figure 6: Mean sections of u_ϕ (cm s^{-1}; scale at right) on the two glider tracks separately (labels at lower right), shown as a function of the cross-Sea coordinate ϕ, from $\phi = 0$ on the Papua New Guinea side to $\phi = 1$ on the Solomons side (section 2.1). The positive direction (red) is equatorward. Data used to construct the sections are shown in Fig. 1. The two green lines separate regions with different sampling periods (section 2.1): Above the green line at 600 m sampling was complete throughout the record (with a single exception); between 600 m and 700 m sampling was complete after the first year; below 700 m sampling began in mid-2013. The time means shown here were computed over each period separately. White contours show isopycnals.

wind vectors, moored buoy wind data, and ERA-Interim model wind fields using a variational analysis to produce four maps daily of 0.25-degree gridded vector winds (Atlas et al., 2011). The CCMP v2 winds are available from July 1987 through May 2016. We constructed daily averages of the (u, v) wind components on a one-half degree grid, then estimated stress assuming constant atmospheric density 1.2 kg m^{-3} and drag coefficient $CD = 1.25 \times 10^{-3}$. Wind stress curl used to force the Rossby model (section 5) was found from these daily stresses, then averaged to monthly values.

2.5. Argo T and S

The Roemmich-Gilson Argo Marine Atlas provides global, monthly-gridded ocean temperature and salinity fields during 2004 to 2016 (Roemmich and Gilson, 2009). The data set consists of Argo-only derived temperature and salinity fields mapped on a 1° by 1° grid, on 58 vertical pressure levels from the surface to 2000 dbar, with vertical resolution coarsening with increasing pressure. The data set can be downloaded from `http://sio-argo.ucsd.edu/RG_Climatology.html`.

We use the Argo Atlas data to describe the temperature variation over the tropical Pacific band as a whole, and to calculate geostrophic velocity referenced to 2000 dbar at the southern and northern edge of the band for the temperature advection calculation in section 6.

2.6. Aviso Sea Surface Height

Multimission satellite altimeter gridded sea surface height (SSH) is computed on a 1/4° by 1/4° daily grid with respect to a 20-year mean (1993–2012) and distributed by the Copernicus Marine and Environmental Monitoring Service (CMEMS; `http://marine.copernicus.eu`). The CMEMS product is known as Aviso ("Archiving, Validation and Interpretation of Satellite Oceanographic data").

We use Aviso data to characterize variability in the Solomon Sea region, especially high-frequency fluctuations that the glider data cannot resolve.

3. Geophysical Sampling Errors

3.1. Intraseasonal "eddies"

Errors due to inadequate sampling of geophysical signals are probably the largest source of uncertainty in the transport integrals shown here (Davis et al., 2012, Appendix). Much of the sampling difficulty stems from the vigorous eddies that have been described several times, from glider data (Gourdeau et al., 2017), satellite altimetry (Melet et al., 2010), and surface drifters (Hristova and Kessler, 2012).

Organized intraseasonal (20–120 days) SSH variability from Aviso (section 2.6) has RMS magnitude as large as its annual cycle variability, and about half the

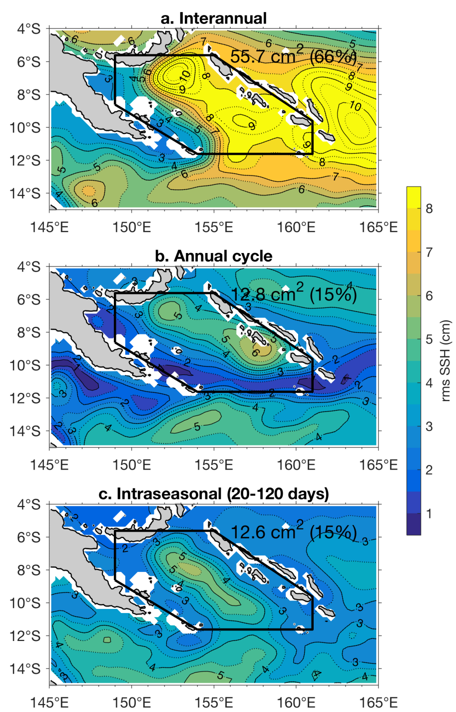

Figure 7: Standard deviation of Aviso SSH split by frequency bands over 2007–2016. The variance averaged over the Solomon Sea in each band is labeled within each plot panel, and expressed as a percentage of total SSH variance over the Solomon Sea. The intraseasonal variance (panel c) is shown decomposed in Fig. 8.

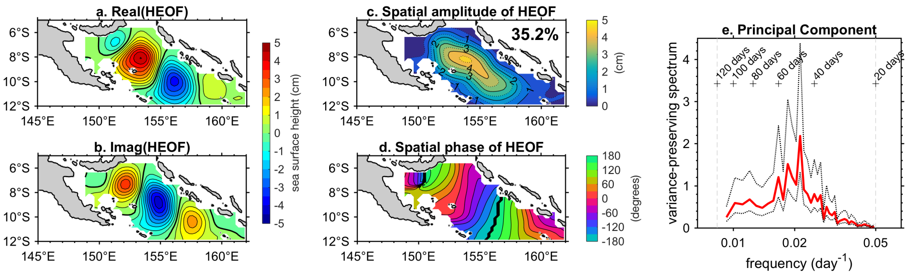

Figure 8: First mode of the Hilbert EOF (see section 3.1) decomposition of Aviso intraseasonal SSH (shown in Fig. 7c), representing 35.2% of the intraseasonal variance. Panels a,b show the real and imaginary part of the oscillatory mode, c,d show the same information but as a spatial amplitude and phase. Panel e shows the spectral peaks of the principal component (red line), with a 95% confidence interval (grey lines).

magnitude of its interannual RMS (Fig. 7). A Hilbert EOF analysis (Horel, 1984) shows that a substantial fraction (35%) of the intraseasonal SSH variance is explained by a single statistical mode. The leading HEOF mode describes a propagating oscillation with a wavelength comparable to the basin size (Fig. 8c,d), westward phase propagation with phase speed 20 cm s^{-1} (Fig. 8d), and spectral peak at 52 days (Fig. 8e). The real and imaginary part of the Hilbert EOF give an alternate view of the mode, showing the propagating oscillation a quarter-period apart – the dominant intraseasonal signal consists of 400 km diameter, basin-filling eddies, of alternating sign, that originate in the southeast corner and propagate west (Fig. 8a,b). It appears that the quasi-stationary cyclonic eddy near Solomon Strait in the northeast Solomon Sea discussed by Gourdeau et al. (2017) is a different phenomenon than the intraseasonal propagating features seen on our southern Solomon Sea glider tracks.

Intraseasonal variability is larger inside the Solomon Sea than in the region to its east (Fig. 7c), suggesting that the basin-filling eddies are generated within the Sea, but the originating mechanism of these features has not been explained. The Hilbert EOF spatial pattern and period suggest the excitation of a basin mode determined by the geometry of the Sea. Indeed, for a rectangular basin of the size and latitude of the Solomon Sea the period for the gravest basin mode is 45–60 days. Resonant basin modes are observed in other tropical locations (e.g., the Celebes Sea; Qiu et al., 1999).

The eddies pose a sampling problem for low-frequency variations, for several reasons: They produce large transport changes on shorter timescales than the present glider sampling strategy can measure, and the intraseasonal geostrophic currents are as large or larger than the speed of the glider through the water, so the glider's path is partly determined by the eddy currents themselves. Occasionally the glider encountered mid-basin currents (i.e., not part of the western boundary jet) strong enough to reverse its progress; these might be indicative of submesoscale vortices (Srinivasan et al., 2017).

3.2. Evaluating sampling with Aviso

We can take advantage of the gridded Aviso fields to investigate transport errors expected from the glider's relatively infrequent sampling, slow motion and irregular path through a vigorous eddy field. A "transport" time series that represents much of the mass transport variability measured by the glider can be derived from SSH gradients by choosing a scale depth to associate geostrophic surface velocity to transport; here we find that a scale depth of 200 m gives the closest least squares fit between glider-measured 0–50 m and 0–700 m transport.

We compare two ways to estimate cross-Sea transport, both constructed from Aviso. "Truth" is based on a simple daily cross-Sea SSH difference. A second "glider-like" measure samples Aviso SSH at the daily-averaged times and locations of each glider dive, finding transport by integrating the resulting cross-track geostrophic velocity segments, resulting in 87 transport estimates with sampling like that of the glider data (Fig. 9). Since both measures are built from surface geostrophy only, the comparison isolates transport errors associated with the glider path and slow passage across the Sea.

Individual mission RMS differences between the "glider-like" measure and "truth", averaged over the durations of each mission (black horizontal bars in Fig. 9) are 5.0 Sv, with maximum difference of 12.9 Sv. Noting the rapid fluctuations of the yellow "daily truth" time series in Fig. 9, it is clear that

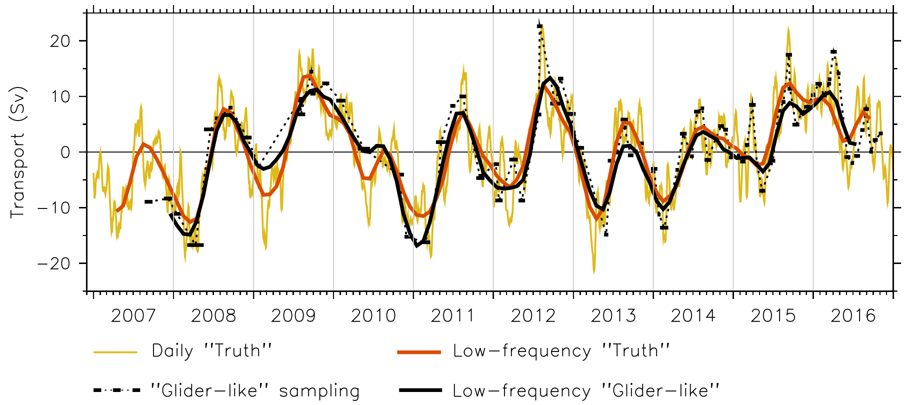

Figure 9: Time series of geostrophic transport anomaly estimates entirely from Aviso (see section 3.2). "Truth" is based on a simple cross-Sea SSH difference, computed daily; "Glider-like" is based on SSH sampled at the times and positions of each glider dive, where the black horizontal bars show the duration of each transect. Since the "glider-like" transport estimates are integrals over a glider path, they do not necessarily fall on the daily "truth" line. Low-frequency estimates include both the annual cycle and interannual anomalies, and were calculated as done for the glider data itself (section 2.2), shown in Fig. 2.

any single glider transect's integral can be significantly unrepresentative of the flow during that transect. However, when the "glider-like" transport measure is piecewise-filled and filtered to low frequencies as was done for the actual glider measurements (section 2.2), the time series demonstrates all the same peaks and troughs as the "truth" measure, with similar magnitude and phasing (Fig. 9). The correlation between "truth" and "glider-like" low-frequency transports from Aviso is 0.93, with RMS difference 2.6 Sv, suggesting that the sampling as done by the gliders adequately describes the low-frequency signals of interest.

This comparison also demonstrates the significance of the technical and operational improvements to the gliders implemented in mid-2013 (section 2.1), that resulted in approximately doubling the number of transects/year with more regular spacing. Before 2013, with an average of 58 days between transects (including a few long gaps that produced especially-large differences), the RMS difference between the "truth" and "glider-like" low-frequency measures was 3.0 Sv. After mid-2013, when the average interval dropped to 26 days, the RMS

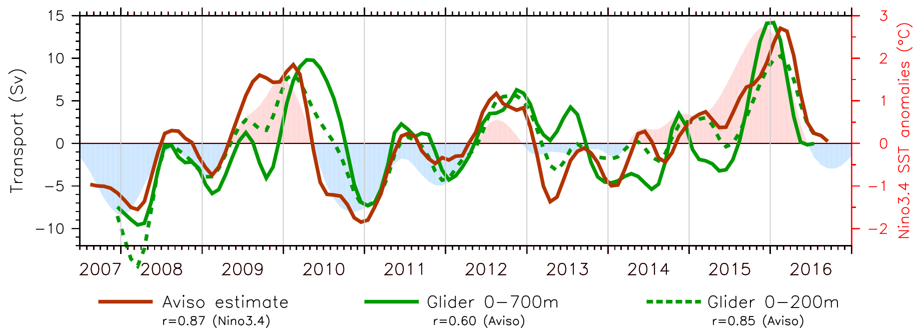

Figure 10: Time series of interannual transport anomaly estimates from Aviso (red) and glider (green). Two estimates were made from the glider data: 0–700 m as used in the rest of the paper (solid), and 0–200 m (dashed) for this comparison only.

difference reduced to 1.8 Sv (Fig. 9).

However, despite more-frequent sampling improving the measurement of low frequencies after 2013, the high-frequency differences between daily "truth" and the "glider-like" time series were virtually the same (3.5 vs 3.7 Sv) across the two sampling regimes. This indicates that the dominant 45–60-day eddies are inherently not well sampled by glider transects that take 20–50 days per transect, even with more frequent sampling.

Comparing the Aviso estimates and in situ glider time series (Fig. 10) shows that an estimate based on SSH reproduces observed interannual transport variability fairly well ($r = 0.60$), though with a notable discrepancy during the El Niño of 2009–10 that will be discussed later.

4. Observed transport mean and variability

4.1. Two separated tracks

The operational need to navigate the gliders in a clockwise route produces separated cross-Sea tracks (section 2.1; Fig. 1). The southern track has two distinct mean velocity maxima: a strong narrow boundary current along the Louisiade Archipelago, about 80 km wide, and a relatively broad mid-basin inflow (Fig. 6, bottom, and Fig. 11). The narrow boundary current is the New

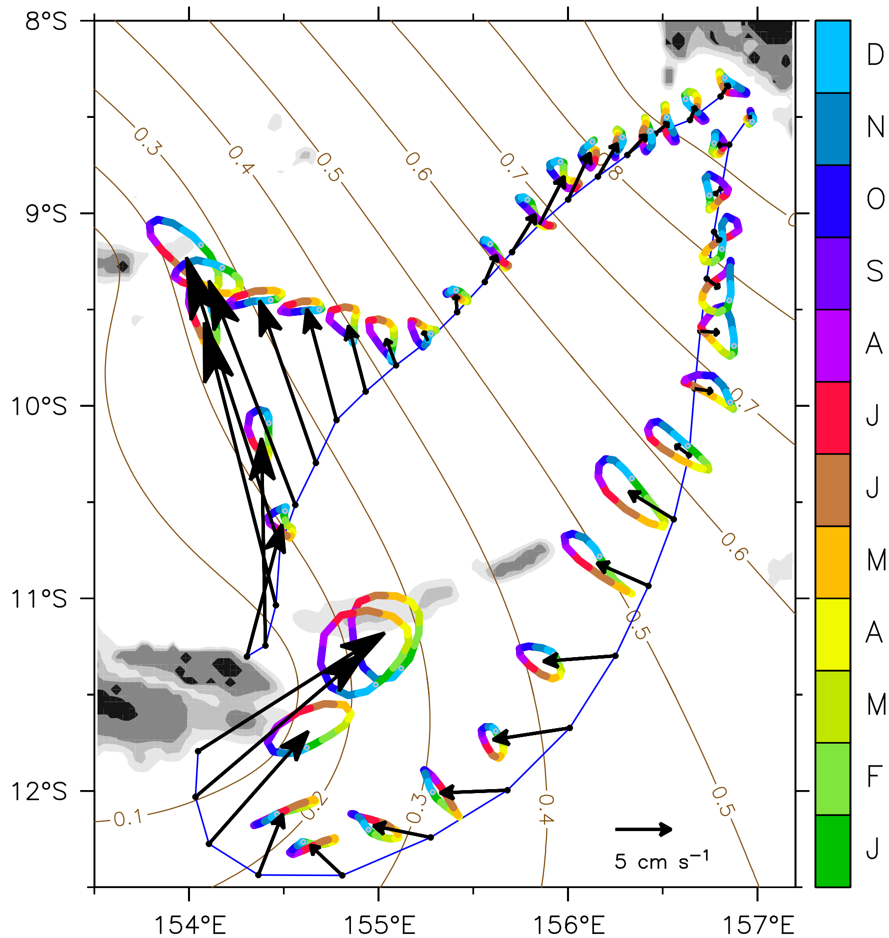

Figure 11: Mean vectors of absolute vertically-averaged velocity (black; scale vector at bottom) on the mean westbound (southern) and eastbound (northern) glider tracks. The colored shapes around each vector head show its direction and magnitude during the climatological year (color scale at right). Brown contours are contours of the cross-Sea coordinate ϕ (section 2.3). Gray shading shows bathymetry at 100 m, 500 m and 1000 m.

Guinea Coastal Undercurrent (NGCU; Lindstrom et al., 1987; Tsuchiya et al., 1989; Sokolov and Rintoul, 2000; Qu and Lindstrom, 2002; Gasparin et al., 2012), and the mid-basin inflow has been identified as the North Vanuatu Jet (Gourdeau et al., 2008; Couvelard et al., 2008; Choukroun et al., 2010; Kessler and Cravatte, 2013a). By contrast, the northern track has a single, broader, maximum on its western side, where the WBC and mid-basin inflows appear to have merged into a single current on the New Guinea side (Fig. 6, top, and Fig. 11).

Vertical sections of u_ϕ (Fig. 6, bottom) show that the southern mid-basin inflow is shallow (above 300 m and surface-intensified), while the NGCU's core is near 400 m depth and is weak or nearly absent in the mean at the surface. The NGCU extends with large magnitude to and below our sampling depths of 700 m or 1000 m (Fig. 6, bottom). Occasional shipboard measurements of the NGCU near Rossel Island confirm this depth extent, suggesting that the current is found to 1500 m or deeper (Gasparin et al., 2012).

It is not known why the deeper parts of the NGCU are apparently weaker on the northern track, potentially a problem with using u_ϕ when the glider track is nearly along-current (see discussion in section 2.3). On both tracks, near-surface flow on the Solomon Island side of the basin is southward in the mean (Fig. 6), though its structure is highly variable (RMS of u_ϕ larger than its mean across this eastern region, e.g., Fig. 11) and is not confidently characterized in the present data. This might reflect dominance of the ubiquitous intraseasonal eddies (section 3.1), or potentially a background southward flow from Solomon Strait.

4.2. Transport time series

The time series of coast-to-coast transport (thin black line with dots in Fig. 2) suggests a strong and regular annual cycle of mass transport; every year has a mid-year transport maximum and a minimum between December and February. Peaks of the average annual cycle are about ± 5 Sv around a mean of 20.2 Sv (green dashed line in Fig. 2).

The absolute velocity provided by the glider is essential to the flow description, especially since the NGCU extends below the glider sampling depth. A geostrophic transport estimate would be a significant underestimate. Mean coast-to-coast geostrophic transport relative to 700 m was only 12.7 Sv, 63% of the absolute transport mean. After mid-2013 when more-capable gliders sampled to 1000 m, mean relative geostrophic transport to that depth was 16.5 Sv, about 70% of the absolute mean. Most of the 700 m or 1000 m dive-bottom signal was in the NGCU at the west end of the transects, where typical crosstrack speeds (u_ϕ) at those depths (what might be called the "reference-level speed") were 25 cm s^{-1} and 15 cm s^{-1} respectively on the southern track and 15 cm s^{-1} and 8 cm s^{-1} on the northern track (Fig. 6).

Interannual transport anomalies (blue line in Fig. 2) span -9.6 Sv to $+14.2$ Sv (thus a large fraction of the 20.2 Sv mean), with an RMS of 5.1 Sv over the 9 years; their largest magnitudes occurred during the large ENSO fluctuations of this record (Fig. 4). Correlation between interannual transport variations and the Niño3.4 SST index are above 0.7 at a lag of about 2 months; with the independence timescale estimated to be about 6 months (via the autocorrelation-product method of Davis (1976)), there are about 18 degrees of freedom in the 9-year record and this correlation is significantly different from zero with a confidence well above 95%. However, note that the timing of the large early-2010 transport peak is uncertain because of the sparse sampling that year (ticks along the time axis of Fig. 4; see discussion in sections 2.1 and 2.2). That peak apparently lagged the Niño3.4 SST peak by about 4 months and thus lengthened the overall highest-correlation lag. We therefore consider the lag relation between Niño3.4 and Solomon Sea transport to remain not well determined and quite possibly not a consistent diagnostic of the connection between ENSO and Solomon Sea flow (see discussion in section 5.2.3).

Large-amplitude annual and interannual transport variability differs between the shallow mid-basin inflow and the much thicker and deeper WBC (Fig. 6). The differences are most clearly seen on the southern glider track where the two elements are well-separated; as mentioned above the inflows appear to have merged soon after entering the Sea.

At the annual cycle, the mid-basin shallow current is maximum in Jul-Oct, while the NGCU maximum has a different timing, in May-Jun (Fig. 11).

At interannual frequencies, the WBC-interior timing difference is most clearly seen in lag correlations between regional transport and Niño3.4 SST (Fig. 12). A

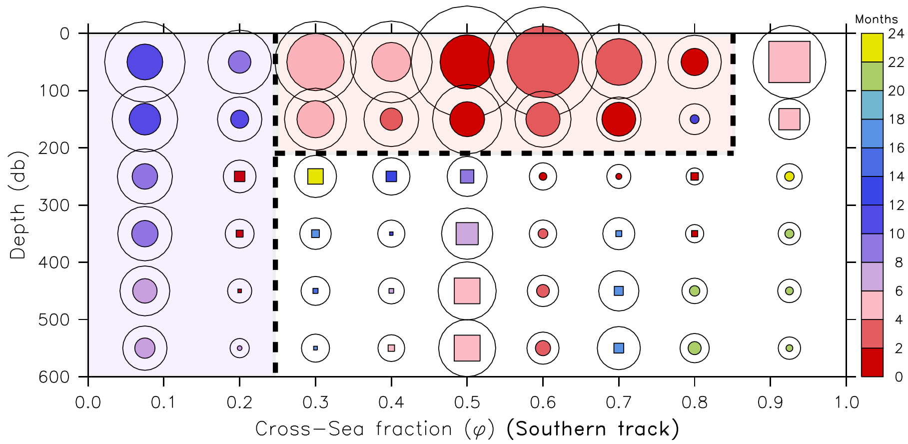

Figure 12: Maximum lag covariances between Niño3.4 SST and glider-measured interannual cross-track transport, binned by depth and by the cross-Sea coordinate ϕ, using the combined tracks. The size of each colored dot shows the covariance magnitude (largest is 0.74 Sv; which can be used as a scale circle), color shows the lag of largest correlation (months; scale at right). The outer black circle shows the RMS transport on the same scale. Circular dots indicate where the highest correlation of transport lags Niño3.4, square dots indicate where transport leads; the two shapes are scaled the same by area. Dashed lines and color shading delineate the regions for comparison with the Rossby model tropical and subtropical solutions (section 5): the western boundary region includes the two columns on the left, while the "shallow interior" is the upper region in mid-basin.

broad region spanning the mid-basin ($\phi = 0.3$ to 0.8) above 200 m depth varies nearly simultaneously or slightly lagged behind Niño3.4, with correlations above 0.4 (about 95% significance), while the narrow, much deeper-extending WBC region against the coast of Rossel Island ($\phi < 0.15$) lags Niño3.4 by 8–11 months with larger correlations (above 0.5). These two elements of large co-variability combine to produce the varying lags seen in total transport (Fig. 4). The roles of these apparently-different signals are discussed further in the context of the linear model explored in section 5 below, and covariances with clearly-defined lags of Fig. 12 to characterize two regions of response. East of the WBC below 200 m, covariances were much weaker, indicating an inconsistent relation between ENSO and Solomon Sea transport in this region (Fig. 12).

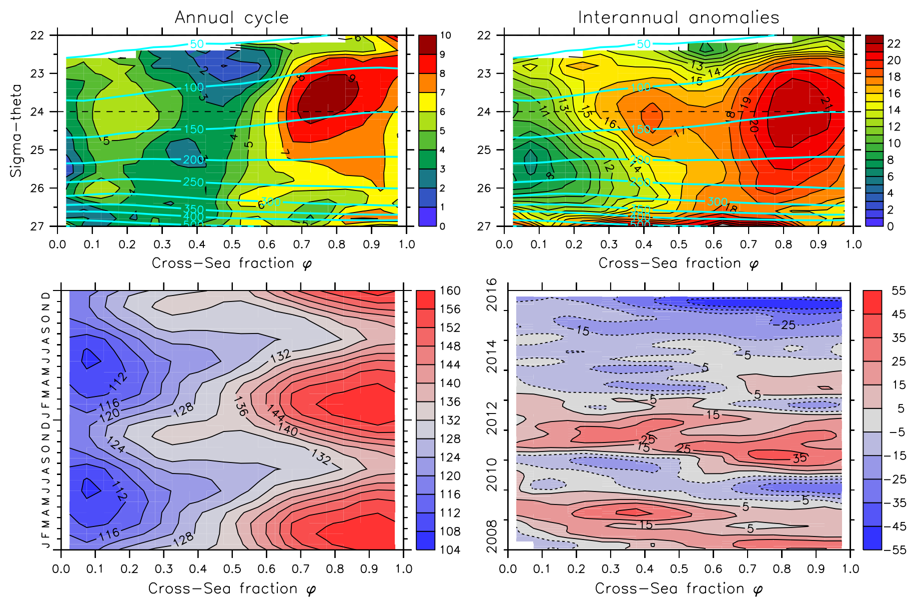

Figure 13: Isopycnal depths across the Solomon Sea from the combined tracks. RMS depths (top panels), observed variations of the depth of sigma 24 (bottom panels). Annual cycle (left panels), interannual anomalies (right panels). All values are meters; each panel has its own scale at right. Light-blue contours in top panels show the mean depths (m) of isopycnals at each ϕ.

4.3. Estimates from Aviso SSH

Consistent with the regionally-varied correlation of transport with Niño3.4 SST (Fig. 12), subthermocline interannual flow variability was weakly anti-correlated with that above 300 m, and episodes of different flow directions above and below the thermocline were common. Although total transport variability was dominated by upper layer fluctuations (that might be seen by Aviso), the magnitude and in some cases the timing of ENSO signals would be misinterpreted by the near-surface variability alone. Glider-measured 0–200 m transport anomalies agree much better with the Aviso estimate ($r = 0.85$; Fig. 10) than those to 700 m ($r = 0.60$). The difference is most apparent during the El Niño of 2009–10, when both the 0–200 m glider transport and the Aviso estimate depict the peak transport anomaly about 3 months earlier than the measurements to 700 m (Fig. 10). This suggests caution in using surface-only measures like satellite SSH to deduce transport anomalies for individual events.

Isopycnal depth fluctuations in the main pycnocline associated with these velocity signals have much larger magnitude on the Solomon Island side, by factors of almost two, for both annual cycle and interannual variability (Fig. 13). A similar pattern was seen in Aviso SSH (Fig. 7a,b). These eastern pycnocline motions drive much of the velocity fluctuations in the central Solomon Sea (e.g., Fig. 11). Reasons for this character of variability are discussed in the next section.

5. A linear wind-driven interpretation of Solomon Sea transport

5.1. Introduction

We do not expect that a linear wind-driven diagnosis will provide a complete explanation of Solomon Sea transport or its fluctuations, but it is straightforward to understand and is an appropriate first guess; at times or locations where the linear diagnosis fails it points to more complex processes or dynamics. The principal advantage of such a model is its linearity, which allows isolating particular elements of the forcing, either in space or frequency. Here, we seek to study the annual cycle and interannual variability independently, and also to separate the tropical and subtropical influences on the transport arriving at the Solomon Sea.

The model dynamics and formulation are described in the Appendix. In brief, the combined model consists of three elements:

- In the interior South Pacific: A first baroclinic mode long Rossby wave anomaly model is driven by either annual cycle or interannually-filtered wind stress (Meyers, 1979; Kessler, 1990; Chen and Qiu, 2004). The output of this model is the thermocline depth anomaly field, which gives the Rossby zonal transport by geostrophy. This zonal transport anomaly arriving at the western boundary is the input to the elements below. Long Rossby waves in this model propagate due west, so solutions are found at each latitude independently and the effects of forcing at any latitude can be isolated.

- Along the coast of Australia south of the Solomon Sea: The arriving zonal transport anomalies are integrated northward, conserving mass in the boundary layer, to form the western boundary current implied by the interior wind forcing (Godfrey, 1975). This defines the subtropical-forced transport arriving at the southern Solomon Sea, and is identified as the NGCU close to the coast of the Louisiades (Figs. 6 and 12).

- Along the east side of the Solomon chain: The Firing et al. (1999) Time-Dependent Island Rule (TDIR) is used to estimate western boundary current anomalies along the east side of the Solomons chain due to the arriving Rossby zonal transport. The TDIR then gives the transport anomalies leaving the southern tip of the chain as a jet extending westward. This jet is the second element of transport entering the Solomon Sea, referred to as the "tropical" forcing, and is identified as the mid-basin shallow transport seen in observations (Figs. 6 and 12).

The model consisting of the above three elements is referred to below as the "Rossby model". Its estimate of transport entering the Solomon Sea reflects only the influence of winds over the interior South Pacific. In particular, winds north of the Solomon chain (5°S), including equatorial winds, or those south of the tip of New Zealand (34°S), play no role (Appendix).

5.2. Linear model results

5.2.1. Mean transport

The Godfrey (1989) Island Rule is an extension of Sverdrup theory to include islands and the circulation to their west (Appendix). The calculation uses only the winds and basin geometry; in this case including the "islands" of Australia-New Guinea, New Zealand, and the nearly-solid Solomon chain. Its output is a single number for each island: the total mean meridional transport

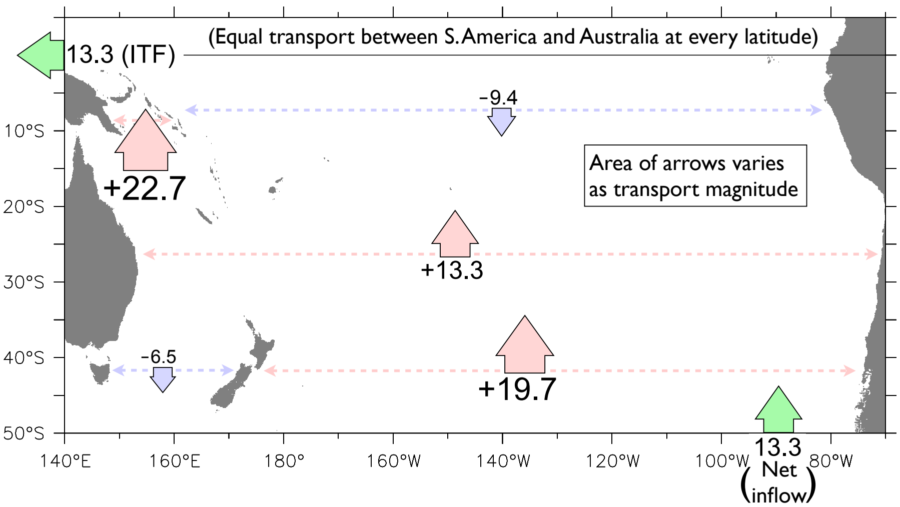

Figure 14: Island Rule meridional transport (including both interior and western boundary currents) between the land mass pairs of South America, New Zealand, Australia and the Solomon Islands. Pink arrows are northward, blue southward, dashed horizontal arrows show the coast-to-coast range represented; green arrows indicate the implied Indonesian Throughflow transport (see section 5.2.1). The area enclosed by each arrow symbol varies as the transport magnitude, with the value in Sv written by the arrow. Total mean transport between South America and Australia is equal at every latitude.

(including both interior Sverdrup transport and WBCs) between the island and the reference coastline to its east (here, South America).

Forced by CCMP v2.0 winds during 1990 through 2016, the Island Rule predicts a mean northward transport of 13.3 Sv at all latitudes between Australia and South America (Fig. 14); this value is therefore also the predicted transport of the Indonesian Throughflow (if Bering Strait is ignored). This estimate is similar to previous Island Rule calculations based on several wind products, which have found ITF transports between about 12 to 15 Sv (Godfrey, 1989; Wajsowicz, 1993), and to observations of the ITF (Sprintall et al., 2009; Gordon et al., 2010).

Considering the two large “islands” east of Australia, the Island Rule predicts a mean of 19.7 Sv flowing north between New Zealand and South America, thus about $19.7 - 13.3 = 6.5$ Sv flowing south in the Tasman Sea. It predicts 9.4 Sv southward transport between the Solomon chain and South America in the tropical cyclonic gyre, which similarly implies 22.7 Sv northward transport through the Solomon Sea (Fig. 14).

This value can be compared with the observed glider-measured transport, keeping in mind that the Island Rule was calculated from 1990–2016 winds, while the in situ observations span 2007–2016. The Appendix explains that even the 27 years of CCMP winds are barely sufficient to describe a meaningful "steady state" assumed for the Island Rule, and in fact the 1990–2016 period has seen strong decadal wind variations (L'Heureux et al., 2013; England et al., 2014).

With that caveat, the glider-measured mean Solomon Sea transport was 20.2 Sv above 700 m (section 4). During the recent 3.5 years with deeper glider sampling, the NGCU was seen to extend to 1000 m (Fig. 6); if that shorter period represents the mean below 700 m it would add another 2.2 Sv for a total 22.4 Sv observed mean transport, similar to the linear Island Rule estimate of 22.7 Sv (Fig. 14).

5.2.2. Annual cycle

Separating the "tropical" and "subtropical" elements of the solution (section 5.1), and associating these with the mid-basin and western boundary elements of observed annual cycle transport respectively (as was illustrated in Fig. 12 for interannual variability), shows a fair correspondence (lower panels of Fig. 15). In both model and observations the shallow interior (Fig. 15b) has about twice the annual transport anomaly magnitude as does the western boundary (Fig. 15c), and in both the western boundary "leads" the interior by several months (but note that "lead" and "lag" in a repeating annual cycle are ambiguous). These phase relations are consistent with the observed shallow-interior vs. western boundary phase differences in Fig. 11.

The phase and magnitude of the complete model solution is nearly identical to that of the total observed transport (Fig. 15a). However, compensating dis-

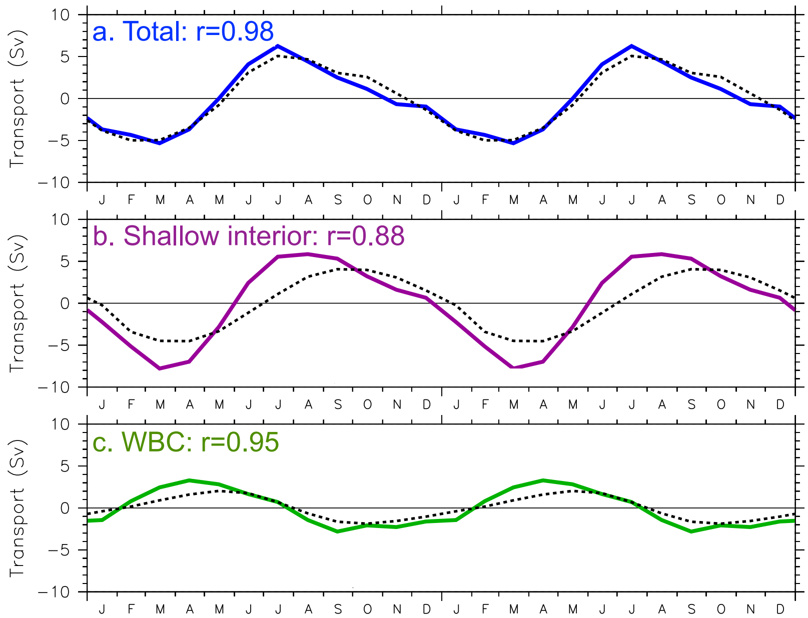

Figure 15: Rossby model prediction of annual cycle transport anomalies entering the Solomon Sea by region. In all panels the black dashed line is the glider-observed transport, colors are the model. Panels show (a) total transport, (b) shallow interior and (c) western boundary regions. For the observations, the WBC and interior observed transports are defined by the high lag correlation regions in Fig. 12, and do not add up to the total in the top panel. For the model, the regions are explicitly the subtropical and tropical solutions (section 5.1). Correlations between the observed and modeled transport are listed in upper left of each panel.

crepancies from the observations in the two components of the Rossby solution sum to a perhaps misleadingly good representation of the total (Fig. 15a). The discrepancies might be due to the model solution yielding an explicit separation of the two elements of wind forcing, while the western boundary vs. shallow-interior distinction we make in the observations is subjective and imprecise, with the limits of each region based on coherent elements of observed variability as suggested in Fig. 12.

5.2.3. *Interannual variability*

The locations of forcing that drive Solomon Sea transport variations is a key question motivating the current work, and that is expected to provide insight into the interannual evolution of the tropical Pacific as a whole. Observed WBC vs. shallow-interior transport variations suggest that the response of the Solomon Sea to ENSO is not simple or consistent among the events (black dashed lines in Fig. 16b,c). One of the four observed ENSO transport signatures is seen especially in the WBC (El Niño peak in mid-2010; also noted in section 4), while two others occur largely or entirely in the shallow interior (La Niña negative anomalies in 2007–2008 and the El Niño peak in early 2016). The drastic transport weakening during 2010 (a 17 Sv low-frequency change over 9 months) was due to a combination of both elements, with the shallow interior leading by about 6 months.

The linear model has some ability to represent these interannual anomalies; its correlation of 0.64 with the observed transport is significant above 95%, though clearly several features are wrong (Fig. 16). The model's overall RMS of 5.4 Sv is similar to the observed RMS of 5.3 Sv, and the same is true for the model's division into WBC and shallow interior elements, suggesting that the separation of wind regions carries useful information about the forcing locations of Solomon Sea transport anomalies. The model correctly reproduces the magnitude and to a large extent the timing of the four ENSO transport signatures during this period: the strong negative La Niña transport anomalies in early 2008 and in 2011, and the El Niño positive anomalies in 2010 and again in late 2015 (Fig. 16a). Notably, the model-predicted interannual transport anomalies are closer to the Aviso estimate (section 3; compare the blue and gray lines in Fig. 16a) than either are to the glider observations, consistent with the idea that the single-active-layer Rossby model is representing the upper-layer flow variations that can be seen in SSH.

The modeled subtropical vs. tropical forcing separation (colored lines in Fig. 16b,c) predicts some of the observed WBC vs. shallow interior differences

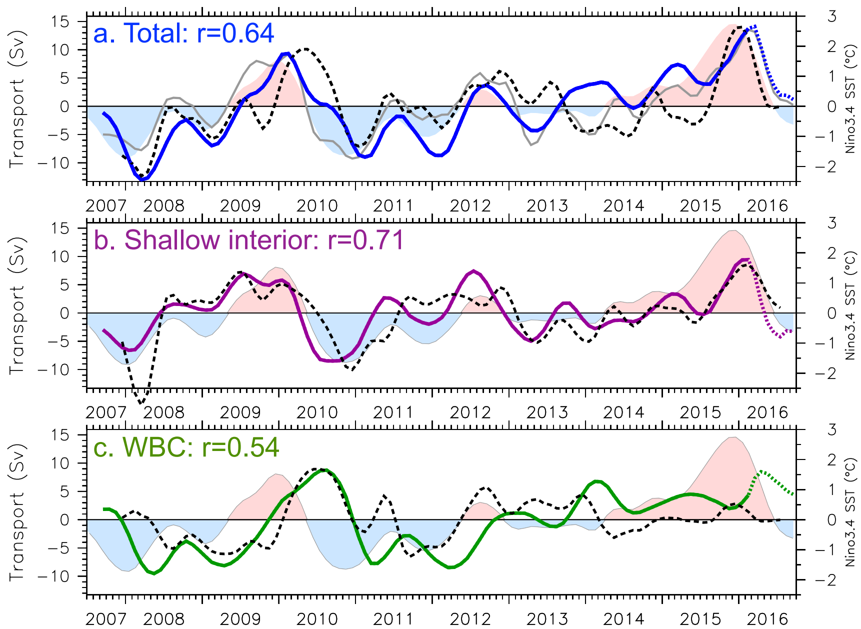

Figure 16: Like Fig. 15 except for interannual transport anomalies, and with Niño3.4 SST indicated by color shading (scale at right). Panel (a) adds a gray line showing the Aviso estimate of total transport from Fig. 10 to compare with the Rossby model estimate (see section 5.2.3). Colored dotted lines at the last 6 months of each model time series are a hindcast (see section 5.2.3).

(dashed lines). The most prominent discrepancy is the response to La Niña in early 2008: while correctly depicted in the total (Fig. 16a), the model suggests that the Solomon Sea transport signal was due about equally to the WBC and the shallow interior, whereas the observations show that the anomalies occurred almost entirely in the shallow interior (Fig. 16b). For the other three large ENSO signals during this period, the model's forcing separation largely agreed with that indicated by the observations, suggesting that the regional forcing distinctions simulated by the model is a useful first guess.

Although the wind product used ended in May 2016 (section 2.4), and the 7-month triangle filter used to construct its interannual anomalies loses 3 months at each end, the model solution contains information about subsequent ocean variability in the Rossby waves remaining at the end of the forced model run. These waves were propagated forward (as if subsequent wind anomalies were zero) to estimate the Solomon Sea transport "predicted" as the waves and the boundary signatures they generate arrive at the Solomon Sea. This was done for 6 additional months, to extend the model solution to Aug 2016, through the decay of the El Niño of 2015–16 (dotted model solution lines at the ends of each time series in Fig. 16). Apparently the waves forced before May 2016 carried information about future downstream variability, suggesting that the rapid transport drop during 2016 was due mostly to changes of the tropical winds in early 2016, not to the WBC.

5.3. Role of local forcing

We noted in section 4 that isopycnal depth fluctuations were much larger on the Solomon Island side, largely controlling the pycnocline slope across the basin (Fig. 13). Disentangling the dynamics driving the slope variability is difficult because the wind fluctuations have large spatial scales spanning the Solomon Sea and regions to its east (Fig. 3). Thus, many features are well correlated or lag correlated with aspects of the forcing and with each other; correlation without a quantitative connection to a mechanism could clearly be misleading in this situation.

Beyond the remotely-forced signals described by Rossby model studied here, two local mechanisms could be important: Ekman transport shifting upper-layer water across the Sea, or local wind stress curl pumping the pycnocline. Solomon Sea winds vary primarily as strengthening or weakening of the prevailing south-easterlies along the SE-NW axis of the Sea (Fig. 3). Stronger winds (mid-year, and with much smaller magnitude during the height of El Niños) move water to their left (westward) by Ekman transport, and pump the pycnocline shallower in the east by upwelling curl east of the mid-basin maximum. Both of these are qualitatively consistent (i.e., correlated) with the observed isopycnal depth fluctuations (Fig. 13), although both would suggest a cross-Sea symmetry of these that is not observed.

Contradicting both of these possibilities, however, the magnitudes of the annual cycle and interannual wind variations are inconsistent with the observed SSH: winds over the Solomon Sea have much smaller interannual variability than annual (Fig. 3a,b), but SSH variability is large at interannual timescales, while having relatively small magnitude at the annual cycle (Fig. 7a,b).

Further, the local mechanisms would suggest an amplitude of isopycnal depth variability a great deal larger than observed. Depth changes implied by Ekman transport can be estimated by assuming that the pycnocline is a material plane that tilts to balance cross-Sea flow anomalies. The cross-Sea Ekman transport is found from the observed winds (Fig. 3 shows that winds are primarily along-Sea so the Ekman transport is cross-Sea). Integrating this transport in time gives the implied volume exchanges between each side of any cross-section; if the surface is assumed a plane then its tilt can be estimated. With these assumptions, upper-layer depth changes due to cross-Sea Ekman transport would approach ± 100 m for the annual cycle, and more than that for interannual variability. However, observed cross-Sea pycnocline depth anomaly magnitudes are less than 20 m and 30 m, respectively (Fig. 13, bottom panels). Implied curl-driven depth changes are smaller, but still several times larger than observed. While the ocean certainly feels this local forcing, it apparently radiates away, pointing to the essential role of wave dynamics.

We have not attempted to run the Rossby model inside the Solomon Sea because its short width, confined basin and complex coastlines are unlikely to be well-represented by a model consisting of wavelengths of thousands of km. However, the TDIR model predicts the pycnocline signal on the west side of the Solomon chain induced by Rossby waves arriving at the east coast. The model assumes that pressure around a "small" island like the Solomon chain is adjusted very quickly relative to the low frequencies of interest; in this case a few weeks (see the Appendix). Thus, the model-predicted west-side pressure is approximately the meridional average of that on the east. One can imagine a long (non-rotating) gravity wave approaching a small rock or island; after a brief transient adjustment sea level on the lee side will soon match that on the exposed side.

We can test the realism of this mechanism using Aviso SSH (section 2.6) that allows characterization of the surface height throughout the Sea, and by the choice of a scale depth (175 m) infer the Rossby-implied SSH displacements. The Rossby model's prediction of pycnocline depth on the western side of the chain (not shown), entirely due to wind forcing east of the Solomons, closely matches the phase and amplitude of observed SSH in the eastern Solomon Sea for both the annual cycle and interannual variations (Fig. 13 shows the pycnocline depth fluctuations). While we cannot exclude a role for local forcing, the remotely-forced Rossby signals passing around the Solomon chain seem to account very well for the SSH variability observed inside the Solomon Sea.

6. The influence of Solomon Sea temperature advection on the tropical Pacific

We have shown that low-frequency variations of Solomon Sea mass transport can be fairly well represented by remotely-sensed SSH differences across the Sea (section 3; Fig. 10). But mass transport is only part of the reason to observe this system. The unique value of in situ measurements in this small regional sea, such as the glider observations reported here, would enable interpreting the downstream effects of Solomon Sea temperature advection on heat content of the entire equatorial strip, potentially a key to ENSO and tropical climate. In this section we take first steps towards quantifying the Solomon Sea equatorward heat transports as part of the overall advective heat balance of the tropical strip.

In general, heat transport through a partial boundary of a domain is not a well-defined quantity for two reasons. First, the zero reference for temperature is ambiguous: integrating anomalies of a flux term like VT over a partial surface, where V is cross-interface velocity and T is temperature at the interface, produces terms multiplied by temperature itself, thus dependent on the choice of reference. Second, a mass flux through a partial boundary either changes the

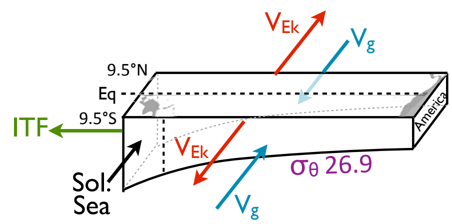

Figure 17: Schematic tropical Pacific box used for the temperature advection calculations (section 6). The red, blue and black arrows indicate the quantities evaluated and are shown in the direction of their mean flow. The ITF (green arrow) could not be evaluated with the data available here, and is treated as a residual.

mass of the domain (thus its heat content), or is compensated by another mass flux (of unknown temperature) through another boundary of the domain.

With these difficulties in mind, Lee et al. (2004) proposed a more limited goal: a technique to compare anomalous temperature advection through a partial boundary with similar measures across other interfaces of the domain. They argued that a unique and suitable reference temperature for this comparison would be the (time-varying) spatial-mean temperature of the volume affected by flow through the interface. They reasoned that advection across a partial interface could contribute to changing the volume's average temperature if, and only if, temperature at the interface differs from the volume average temperature at that moment. The Lee et al. (2004) method provides an estimate of anomalous temperature advection across a partial interface that can be compared with similarly-estimated advection across other elements of a domain's boundary surface, even if the mass balance of the domain is unknown.

Here, we compare the effect of advection by Solomon Sea currents to advection across other interfaces of the tropical strip (see the schematic in Fig. 17), and to the rate of change of temperature of the strip as a whole. The calculation is not a heat balance or budget, but it allows assessment of the relative effects of advection by the several potential sources on the timing and magnitude of temperature changes within the tropical strip.

With the above stipulations, the advective temperature flux through a partial interface A is meaningfully defined by the integral

$$-\int_A V \cdot n(T - T_m)\, dA/V_D \tag{3}$$

where A is a partial interface of a domain D, which has volume $V_D(t)$ and volume-average temperature $T_m(t)$, dA is an infinitesimal element of A, with perpendicular (outward) unit vector n. $V(t)$ and $T(t)$ are evaluated in each grid-cell of the interface.

Domain D was defined as the tropical strip within 9.5°S–9.5°N above σ_θ 26.9, approximately the deepest isopycnal sampled by every glider mission (mean depth over D about 450 m). All calculations reported in this section were repeated with a fixed bottom depth of 500 m, defining vertical velocity at this depth to be $w \approx (\Delta\rho/\Delta t)/(\overline{\Delta\rho/\Delta z})$; interannual temperature advection results were indistinguishable from those derived from the isopycnal bottom. Given the near-equivalence of the two domain choices, we chose to present the isopycnal bottom since interpretation of the temperature advection terms is simpler and more physically direct.

Mean T_m estimated from the monthly Argo Atlas in domain D was about 15.8°C. Its annual cycle was weak, and its interannual variability varied over a range of about ±0.2°C, higher shortly before El Niños and lower shortly before La Niñas. $T_m(t)$ measures much the same quantity as "warm water volume", the area-averaged depth of the 20°C isotherm often used for ENSO diagnostics (Meinen and McPhaden, 2000; Kessler, 2002; Xue et al., 2017); thus the few-month lead of $T_m(t)$ on ENSO measures is similar. Volume V_D varied by about ±1% of its mean, much of which was a slow downward trend from 2007 to 2011, then an upward trend to 2016, with relatively little interannual variability.

All data used for the calculation of V and T in (3) were monthly values of low-frequency filtered velocity and temperature on the surfaces of the box, where "low-frequency" includes the average annual cycle plus interannual anomalies (section 2.2). Three faces (Fig. 17) of the domain were evaluated: Two were long zonal transects, along 9.5°N from Mindanao to Central America, and along 9.5°S from the Solomon Islands to South America. Both of these were calculated from the Argo Atlas for the geostrophic flow and advected temperature, and CCMP winds for the Ekman velocity, assumed to be a slab layer 75 m thick. The third transect was across the Solomon Sea, where glider data defined the absolute geostrophic velocity and temperature, and again CCMP winds gave the Ekman velocity. Volume-mean temperature T_m and its advection into all three outward-facing surfaces of D were evaluated from the isopycnal 26.9 to the surface. We assume no heat transport across the isopycnal bottom of D, but its depth (and thus volume V_D) varied. Each element of cross-interface velocity was associated with the temperature of the water it advects.

Mean Ekman and geostrophic temperature advection partially canceled when summed across the long faces of the tropical box, including the Solomon Sea (Fig. 18). On average, both elements transported water warmer than T_m, since the Ekman outflow occurs near the surface, and the geostrophic inflow largely at thermocline depth and above. While the mass transports of the two elements are nearly equal and opposite, the somewhat warmer temperature of the Ekman-advected outflow made its magnitude of temperature advection larger than that of the geostrophic inflow by about one-third. The net effect of the horizontal advection terms cooled the tropical domain by about $-0.03°\mathrm{C}\ \mathrm{month}^{-1}$ during 2007–2016 (brown curve in Fig. 18). This must be balanced by a combination of surface fluxes, advection in the ITF, and also represents errors, especially our likely underestimate of the Mindanao Current (which as a shallow equatorward current transporting water warmer than the volume mean would tend to reduce the net cooling estimated here).

At the annual period, Ekman advection dominated the weaker geostrophic signal, and overall advective cooling of the domain was much stronger in boreal winter (Fig. 18); the stronger annual amplitude of northern hemisphere trade winds determined the phase of the Ekman advection seasonal cycle, and thus of total advection. Variability of the individual geostrophic and Ekman terms was large on timescales longer than ENSO, but had some cancelation on these timescales (Fig. 18). The interannual sum (net advective tendency; brown curve in Fig. 19a) primarily expressed typical ENSO periods, leading Niño3.4 by about

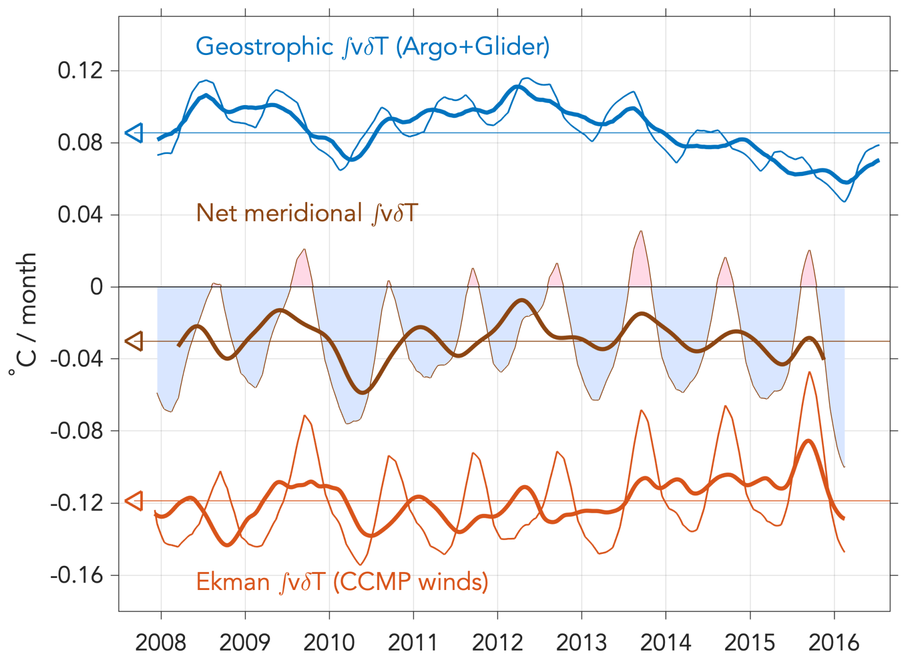

Figure 18: Meridional temperature advection terms (°C month^{-1}) for the northern plus southern sides of the box in Fig. 17. $\int v\delta T$ is shorthand for the advection term (3). Positive values indicate warming tendencies. Blue lines show geostrophic temperature advection, red lines Ekman; thin lines are monthly observed values, thick lines are interannually filtered. Triangles at left indicate the mean of each curve. Net meridional advection (sum of the geostrophic and Ekman elements) is shown in brown, its monthly values are shaded blue for cooling, pink for warming, while the thick brown line is interannnually filtered. Its mean is equivalent to a net cooling of 0.03°C month^{-1}.

6 months ($r = 0.59$).

As a matter of sampling, volume-average temperature in the equatorial strip T_m is effectively independent of the advection terms found here, so comparison of observed dT_m/dt with estimated temperature advection (3) integrated over the faces of the box is a fair test of the method (Fig. 19a). Despite the calculation's relative crudity, the agreement in interannual magnitude and phase of these terms suggests that, first, horizontal temperature advection is a principal effect on interannual temperature variations of the volume, and second, the

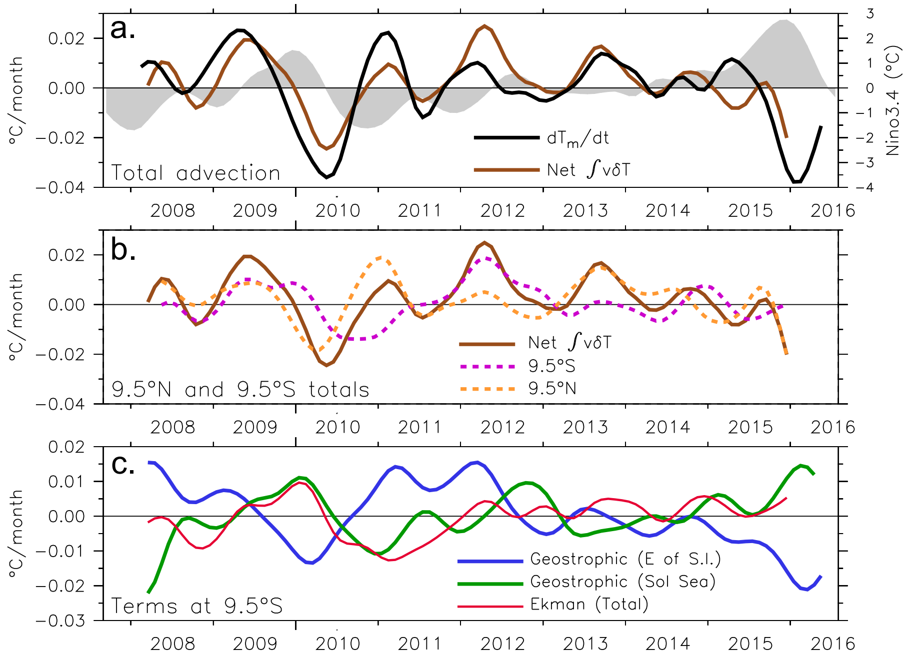

Figure 19: Interannual anomalies of temperature advection terms ($^\circ$C month^{-1}) for the arrows shown in Fig. 17. a: Rate of change of temperature dT_m/dt in the tropical strip (black; section 6) and total advection through all box faces (brown). Niño3.4 SST anomalies are shown by the gray shading. b: Contributions to advection from the southern (orange) and northern (purple) faces of the box in Fig. 17, and the sum (brown; same as panel a). c: Elements of the southern term separated into east (blue) and west (green) of the Solomons chain, along with the basinwide Ekman contribution (red).

Lee et al. (2004) method provides a useful diagnostic of this important influence on tropical Pacific heat content. Interannual advection represented about two-thirds the magnitude of total rate of change of temperature in the box (Fig. 19a). By contrast, annual cycle advection, dominated by northern hemisphere Ekman transport, was poorly related to observed annual cycle dT_m/dt (not shown), which displayed a semi-annual signal, perhaps related to the solar forcing.

Surprisingly, neither northern or southern faces of the tropical box had a consistent relationship with each other or with ENSO during this period (Fig. 19b). The time series of temperature advection integrated over each face provides several examples of different behavior, suggesting that there is not a regular or typical subtropical advective signal in response to ENSO wind anomalies. Nor was there a consistent contribution to the "recharge" (Jin, 1997; Ishida et al., 2008) preceding El Niño events: the 2009–10 El Niño followed a large advective temperature increase by about 6 months, but the 2015–16 event had little sign of increased temperature advection (Fig. 19b); though it is worth noting that only a small increase in spatial-mean temperature of the equatorial strip preceded that event (Fig. 19a).

The opposing effects of western boundary and interior-basin advection across 9.5°S followed expectations, with both terms highly lag-correlated with ENSO (Fig. 19a): the interior ocean east of the Solomons drained warm water from the equatorial strip in the few months following the El Niño peak, while flow through the Solomon Sea added about the same amount a few months later (Fig. 19c); La Niña did the opposite. Overall, the Solomon Sea contribution to interannual temperature advection was oppositely-signed and almost as large as that east of the Solomon chain all the way to South America, for every interannual perturbation of this period. In fact all the terms summarized by the five meridional arrows in Fig. 17 had similar interannual magnitude (e.g., Fig. 19b,c), suggesting that monitoring the heat transport of all these influences will be necessary to describe the evolving climate of the tropical Pacific; both velocity and temperature measurements will be required.

7. Summary and discussion

An earlier paper described the first 3.5 years of glider observations (Davis et al., 2012); its conclusions are largely borne out by the much longer time series and more complete sampling studied here. New observational findings include large differences in velocity structure between the southern and northern transects serendipitously enforced by the glider's operational requirements (Fig. 1;

section 4). The two previously-identified sources of inflow to the Solomon Sea (the shallow mid-basin inflow and the narrow, much vertically-thicker western boundary current; Fig. 6) merge to combine mass and properties shortly after entering the Sea (Fig. 11). This suggests that at least some of the mixing of tropical and subtropical thermocline waters noted as occurring in the Solomon Sea (Alberty et al., 2017; Ganachaud et al., 2017) could be a consequence of this merging close to the mouth of the Sea.

The time series of glider transects across the Solomon Sea now spans two El Niños and two La Niñas (Fig. 4). While in general the El Niños produced large transport increases and La Niñas decreases (anomaly magnitudes more than 50% of the mean transport), ENSO signatures were inconsistent among the events in timing and lag relation with equatorial ENSO indices (section 5). In general the signals appeared first in the shallow mid-basin inflow, and later in the WBC, but the mix of anomalies among these varied considerably among the events.

Gliders have proven to be a viable technique for sustained monitoring of the transport and characteristics of fast, narrow boundary currents in remote locations where other technologies would be difficult to implement. They are especially useful where spatial resolution of a few km, and the combination of property and velocity measurements, is needed. Comparing the glider transport time series to measures of cross-Sea pressure differences, such as those obtained from satellite altimetry or endpoint moorings (Roemmich et al., 2017; Anutaliya et al., 2019), show that pressure alone gives some skill as an index of low-frequency transport variability, but in the Solomon Sea can miss important subsurface velocity signals (section 4; Fig. 10). The high temporal resolution of pressure measurements is useful in evaluating sampling errors of the much-slower glider, and was key to our realizing that the initial roughly six transects/yr was insufficient to describe the low-frequency signals of interest (section 3; Fig. 9).

The simplest possible time-dependent dynamical model expresses the effects of the linear wind-driven circulation, acting through mass-conserving western boundary currents, on flow entering the Solomon Sea (section 5). Despite its simplicity, the model was able to describe the annual variability of transport quite well (Fig. 15), and much of the interannual fluctuations. Its interannual representation was better for the shallow interior flow (Fig. 16b), which might have been expected since this is due to depth fluctuations of the tropical thermocline that such a model is designed to simulate. These tropical dynamics appear fundamentally less complex than those of the much thicker western boundary current whose forcing extends well into mid-latitudes. The model results suggest that the two elements of flow entering the Solomon Sea are driven largely independently (Fig. 12) by wind variations in the tropical and subtropical bands, respectively.

The linear model proposes an answer to the long-puzzling question (Gasparin et al., 2012; Kessler and Cravatte, 2013a,b) of why shallow flow from the tropics turns north into the Solomon Sea, even though wind stress curl is always strongly negative across the mouth of the Sea. The TDIR (see Appendix) distributes incoming zonal transport along the eastern coast of an island into zonal jets extending westward from the island's tips (Godfrey, 1989; Firing et al., 1999). When the jets' transport arrives at the next boundary to the west, it is incorporated into that land mass's western boundary current; this process is not driven by local wind stress curl or other local forcing. In this case the jet from the southern Solomons joins the arriving boundary current from the subtropics soon after they both enter the Solomon Sea. This picture is consistent with the glider observations showing that the structure of flow entering the Solomon Sea has two separate currents that are distinct in the southern glider track but have largely merged by the northern one, only a few hundred km inside the Sea (Fig. 11).

In the introduction, we argued that the Solomon Sea's large (> 20 Sv) northward mean transport was a consequence of the open Indonesian Throughflow. In the mean, the linear Godfrey (1989) Island Rule correctly predicts ITF transport, and also gives an excellent estimate of the mean transport through the Solomon Sea (Fig. 14). Apparently, the large mean mass transport through this small regional sea is forced by winds over the entire South Pacific acting through primarily linear dynamical processes.

The full potential of in situ LLWBC observations will be reached when velocity and temperature measurements can be combined to describe the LLWBC contribution to the evolving subtropical-equatorial heat exchange that is crucial to ENSO and longer-timescale signals along the equator. This description will be essential to understanding the role of the LLWBCs in the tropical climate. We have taken an exploratory initial step towards that goal here, with results suggesting that western boundary temperature advection, in particular through the Solomon Sea, is a first-order contributor to interannual temperature variations across the equatorial band (section 6; Fig. 19). This calculation suggests the power of the method, though without corresponding measurement of the other LLWBC (Mindanao Current in the North Pacific) and the Indonesian Throughflow, the full picture will remain uncertain. In general, the relation of LLWBC temperature advection to ENSO wind forcing is, unfortunately, not simple, and appears to require ongoing in situ monitoring to characterize.

We had hoped after a decade of glider observations to be able to establish a clear timing of the Solomon Sea signal in relation to ENSO indices, and thus to describe consistent aspects of the Solomon Sea current system response to ENSO. Neither of these hopes were fully realized (section 4; section 5.2.3). While some of the uncertainty might have been due to inadequate sampling in the period before 2013 (section 2.1), it appears that the ENSO signal in the Solomon Sea manifests differently for different events, as ENSO does in many of its other features (e.g., McPhaden et al., 2015); clearly, long records will be required to unravel these effects. The fact that the linear Rossby model – with some skill in depicting observed transport variations and their locations and features (section 5.2.3) – shows a similar lack of consistent ENSO manifestation suggests that the complexity we observe is present even in the simplest linear wind-driven dynamics.

Acknowledgements

We thank Solomon Islanders Danny and Kerrie Kennedy, Wryne Lingisasa, Irving Eddie, John Vao, and Bradley Taino who expertly and safely captain the small boats for glider deployments and recoveries. Chanel Iroi and David Hiriasia of the Solomon Islands Meteorological Service help us navigate the politics of working in this emerging nation and find opportunities to return the hospitality its people have shown us. United States Consular Agent Keithie Saunders explains and resolves countless issues of clearances, customs and kastom; without her deep understanding of these islands this project would not be possible. Scripps IDG development leader Jeff Sherman designed the Spray glider, advised on all aspects of the fieldwork, and navigated the glider. Scripps IDG field engineers David Manley, Kyle Grindley, Evan Goodwin and Ben Reineman skillfully built and deployed 37 gliders in difficult field conditions without a single loss. Many colleagues in the vigorous Solomon Sea community gave us useful and interesting criticism, including Sophie Cravatte, Janet Sprintall, Dean Roemmich, and Alex Ganachaud. CCMP Version-2.0 vector wind analyses are produced by Remote Sensing Systems; the wind data are available at `www.remss.com`. Aviso sea surface height anomaly fields are processed and distributed by the Copernicus Marine and Environmental Monitoring Service (CMEMS), with data available at `http://marine.copernicus.eu`. Argo data were collected and made freely available by the International Argo Program and the national programs that contribute to it (`http://www.argo.ucsd.edu`, `http://argo.jcommops.org`). The Argo Program is part of the Global Ocean Observing System. Funding for the gliders' fieldwork and operational expenses was provided by NOAA's Ocean Observation and Monitoring Division, and the glider data that went into this study is available at `http://spraydata.ucsd.edu/projects/Solomon`.

Appendix A. A linear wind-driven model for Solomon Sea transport

We do not expect that a linear wind-driven diagnosis will provide a complete explanation of Solomon Sea transport or its fluctuations, but it is straightforward to understand and is an appropriate first guess. For the time-dependent linear solutions studied here we make the simplification of considering only a single active layer, with adjustment timescales of the first baroclinic mode: months to years at latitudes spanning the subtropical gyre. Such a model neither exploits nor explains anything about patterns of ocean properties; the model ocean is defined only by its basin geometry and mean stratification, the only forcing is the wind stress, and the only output of the model is the mass transport field.

Mean dynamics. In a closed basin like the North Pacific, mean coast-to-coast meridional transport must be zero, so in the linear case the mean western boundary current (WBC) balances the interior Sverdrup transport at each latitude.

As mentioned in the Introduction, the existence of the Indonesian Throughflow (ITF) requires a net northward transport through the South Pacific of about 15 Sv that does not obviously depend the wind stress forcing over the basin. In such an ocean with net meridional flow, if that total transport is unknown the Sverdrupian method cannot deduce the western boundary flow. The Godfrey (1989) Island Rule provides a means of quantifying the effects of the open ITF on South Pacific circulation.

Godfrey (1989) extended the theory of Sverdrup (1947) to encompass islands, thus taking account of the circulation around Australia (Lee et al., 2002; Ridgway and Dunn, 2007; Sprintall and Révelard, 2014) and broadening the Sverdrup diagnosis to the Indo-Pacific as a whole; the convincing demonstration of his "Island Rule" was its correct estimate of Indonesian Throughflow (ITF) transport based on observed winds and basin geometry alone. The dynamics are assumed purely Ekman plus geostrophic (i.e., Sverdrupian) everywhere except in thin western boundary layers, where an unspecified alongshore "friction" is added, as a feature only of strong coastal currents. Alongshore WBC transport is assumed purely geostrophic, depending only on the coast-vs-offshore pressure difference. Godfrey's result has been repeated several times with similar success (Qiu et al., 2009).

Here, we compute the Island Rule transport for the "islands" of Australia-New Guinea, New Zealand, and the Solomon chain, using mean CCMP v2 winds from 1990 through 2016. Results are reported in section 5.2.1. Note that the Island Rule transport between Australia and South America is necessarily also the transport of the Indonesian Throughflow.

The Island Rule calculation depends on two terms: the meridional-average Sverdrup transport in the area to the east of the island, and the circum-island integral of the alongshore wind stress (scaled by the difference in the Coriolis parameter f between its northern to southern tips):

$$T_0 = \overline{T_{Sv}} + \frac{1}{f_N - f_S} \oint_{Island} \tau^l \, dl \tag{A.1}$$

where T_0 is the total northward transport between the island and the coast to its east (a constant), $\overline{T_{Sv}(y)}$ is the meridional Sverdrup transport $V_{Sv}(x, y) = Curl(\tau)/\beta\rho$ integrated west to the island, with the overbar indicating an average over the latitude range of the island, and τ^l is the alongshore wind taken positive clockwise around the island along coast distances dl (Godfrey, 1989). The first term of (A.1) is usually far larger than the second "circum-island" term, even for large islands like Australia and New Zealand, because the around-island integration often incorporates cancelling winds.

With T_0 found, the WBC transport at each latitude is the difference between T_0 and the Sverdrup interior transport $T_{Sv}(y)$ just offshore, thus the WBC meridional profile is straightforwardly calculated from (A.1). Transport of the WBC at the island tips feeds or is fed by jets that extend westward from each tip, thus passing the latitude-mean T_0 to the next coastline to the west.

Equation (A.1) suggests a fundamental difference between the WBC in a meridionally-open basin (that can carry a net transport) from that in a closed one, where the Sverdrup transport at each latitude is balanced by the WBC. Neglecting the circum-island term for the moment shows that the WBC against the east coast of an island is due only to the variation of T_{Sv} with latitude. If

T_{Sv} is constant in y (with T_0 a constant for each island), then $T_{Sv} = T_0$ at all latitudes; the Sverdrup flow carries the entire transport in the interior ocean east of the boundary layer and there will be no WBC. This view emphasizes the role of zonal inflows to the WBC, because the Sverdrup zonal transport at the island's east coast is $-dT_{Sv}/dy$, i.e., occurring only with meridional variation of T_{Sv}.

The circum-island term is relatively important in the case of the Solomon chain, because southeasterly winds are stronger inside the Solomon Sea than in the Pacific to its east (Fig. 3); this term results in a net clockwise flow around the Solomons, contributing a southward mean WBC of about 2 Sv along the east side of the chain. Note that no corresponding eastern boundary current is called for in the Godfrey (1989) formulation. In the hypothesized weak currents along the west side of an island, alongshore winds are balanced by an alongshore pressure gradient; in the case of the Solomons the strong southeasterly trades inside the Sea are balanced by higher pressure at the northern than southern tip. Along the east side of the chain the resulting tip-to-tip pressure gradient is a southward contribution to the WBC according to the second term on the right side of (A.1).

Time dependence. A time-dependent linear solution for anomalous transport entering the Solomon Sea, thus comparable to the glider measurements reported here, can be constructed from three elements: An interior Rossby wave model driven by observed winds, and two western boundary solutions (separately for the coast of Australia and for the Solomon chain) whose input is the zonal transport resulting from the interior Rossby model. These elements are described below.

In the interior ocean east of the western boundaries, a single-active-layer long Rossby wave model (Meyers, 1979; Kessler, 1990; Chen and Qiu, 2004) is forced by CCMP winds (section 2.4) during 1990–2016. The dynamics are Sverdrupian in retaining only Ekman and geostrophic velocities that are assumed to be in steady balance with the wind forcing and interface slope at each instant, but add a term representing slow evolution of the interface depth, which allows the system to evolve in time and Rossby waves to propagate. The Rossby model is the simplest time-dependent modification of the Sverdrup balance.

Two potential sources produce long Rossby waves in the extra-equatorial South Pacific: those generated by interior wind stress curl (which the model used here is designed to represent), and waves emanating from the coast of South America. These could be specified as a time-dependent eastern boundary condition, or produced by an equatorial model (which this model is not), but theoretical, observational and model results suggest that such boundary-reflected waves are a small part of the solution at the western boundary across 15,000 km of ocean (Kessler and McCreary, 1993; Minobe and Takeuchi, 1995; Fu and Qiu, 2002; Vega et al., 2003). We therefore approximate this by specifying a zero eastern boundary condition for the Rossby model.

The Rossby model solution is the interior thermocline depth anomaly field, which gives the Rossby zonal transport anomalies $U_{RW}(y,t)$ by geostrophy. The relevant output of the Rossby model here is $U_{RW}(y,t)$ arriving at the western boundary: from central Australia to the Solomon Sea, and along the east coast of the Solomon chain. Annual cycle and interannual anomaly runs of the Rossby model were made, both forced by CCMP winds.

Along the east side of the Solomons chain, we use the method of Firing et al. (1999), who showed how a Rossby wave model could be extended to describe the time-varying western boundary current along the east coast of an island, applying this to the east side of the Hawaiian chain. Firing et al. (1999)'s "Time Dependent Island Rule" (TDIR) looks at WBC transport as forced by zonal transport anomalies arriving at the boundary layer, and provides a simple rule for distributing the incoming transport into the WBC. Again it includes a circum-island term and a usually-larger term reflecting the zonal inflows at each latitude along the island's east coast.

The TDIR rule is "in the absence of circum-island wind an inflow to the boundary current at latitude y will split, with fraction $(y-y_S)/(y_N-y_S)$ going north and the remainder going south", where subscripts S and N refer to the south and north tips of the island (Firing et al., 1999).

The rule is appropriate only for "slow" variations of this transport, where "slow" implies that the timescale of interest is much longer than the adjustment time of pressure around the island (via baroclinic coastal Kelvin waves). For small islands such as the Hawaiian or Solomons chain, the adjustment time is a week or so, and the TDIR provides a means of calculating the anomalous WBC from the incoming zonal transport implied by the long Rossby model described above.

While most studies using the TDIR have focused on the WBC on the east side of an island (Firing et al., 1999; Fernandez et al., 2014; Chen et al., 2014; Yamagami and Tozuka, 2015), here we are interested in the flow west of the Solomon chain, entering the Solomon Sea. The northern and southern endpoints of the island's WBC must, in the long Rossby context, produce anomalous jets extending westward from the island tips, so here we calculate the TDIR-predicted transport of those jets. In this linear formulation, the northern jet can have no impact on the Solomon Sea southern entrance, so the TDIR contribution to Solomon Sea transport measured by the glider is the jet from the south tip of the Solomons, which incorporates forcing east of the Solomons chain over the latitudes 5°S–11.5°S (weighting transport in the southern part of this range higher according to the TDIR rule stated above). Meridional transport variations due to wind stress curl inside the Solomon Sea are also included in the "tropical" term here (note that the short zonal extent of the Sea allows adjustment much faster than the timescales of interest, so a simple Sverdrup transport estimate is appropriate); its annual and interannual anomalies are about 1/5th as large as the TDIR terms.

The TDIR solution here feels winds only over the latitude range of the Solomons, and is referred to as the "tropical" contribution. We will identify this as the observed shallow mid-basin inflow to the Solomon Sea described in section 4.1.

Although one might seek a similar TDIR solution for the WBCs along the east coast of Australia-New Guinea, thereby describing the second element of flow entering the Solomon Sea, it is important to note the difficulties in trying to apply a time-dependent rule to this much larger land mass. In the simplest case, the coastline distance around the "island" is about 25,000 km, so the fastest baroclinic coastal Kelvin wave would take at least 100 days to circle the island, not strongly separated from the annual or interannual timescales studied here (and many geographical and bathymetric complications would slow or disperse such a wave). But because the northwest tip of New Guinea touches the equator, a coastal wave approaching that point would partly reflect as an equatorial Kelvin wave, which would travel east along the equator and then reflect as Rossby waves emanating from the entire American coast, eventually coming back to Australia and spawning further coastal waves. The timescale of this adjustment would be a decade or longer. This limitation to very long timescales applies to any estimate of the wind-driven circulation around Australia-New Guinea, either by using the Godfrey Island Rule to estimate the mean over periods less than decades, or using the TDIR for its variability. It does not make physical sense to assume that a diagnosis based on short periods would yield useful information about the Sverdrup circulation of the Indo-Pacific.

Nevertheless, estimating the transport entering the Solomon Sea requires a time-dependent estimate of the contribution arriving from the subtropics. Giving up on calculating this in its full complexity, we take a tractable alternative by choosing a poleward boundary condition for the anomalous WBC along the coast of Australia somewhere south of the Solomon Sea. In effect, for this purpose we assume that Australia is a continent with a known WBC at a particular latitude. By choosing the WBC to be zero at that latitude, the results here are relative to that point.

Along the coast of Australia south of the Solomon Sea, the WBC is defined using a method due to Godfrey (1975), again with its input the Rossby zonal transport $U_{RW}(y,t)$ resulting from the interior Rossby model described above. Since the EAC is known to become dominated by eddy transport as it flows south (Ridgway and Godfrey, 1997; Mata et al., 2000; Ridgway and Dunn, 2003), the southern limit for a linear calculation should be north of about 30°S; here we use 24°S, a relatively quiet region in the lee of New Caledonia. The chosen zero boundary condition was tested at latitudes from the Tasman Front (near 30°S) to the Coral Sea, with relatively small sensitivity at annual to interannual timescales, as long as the Coral Sea latitude range is included (by choosing a starting point south of approximately 20°S).

The anomalous WBC is found as the equatorward integral of incoming transport $-U_{RW}$ from the chosen poleward-side zero boundary condition to the latitude of the Solomons. This integration expresses conservation of mass in the boundary layer: At each latitude and time step, mass conservation is satisfied by propagating the net transport (the arriving U_{RW} at that latitude plus whatever has been accumulated from further south) northward along the coast (Godfrey, 1975). The integral is northward because coastal Kelvin waves travel equatorward along a western boundary, so information on this coast can only go north. With the travel time of a first-baroclinic-mode coastal Kelvin wave being less than 10 days along the 2000 km eastern coast of Australia, we assume this propagation is instantaneous. The result of the integration is a time-varying WBC transport arriving at the southern opening of the Solomon Sea at 11.5°S. This incorporates wind forcing over the subtropical gyre, and is the linear mechanism by which Solomon Sea mass transport feels subtropical wind anomalies. Since this signal arrives at the Solomon Sea as a western boundary current, we identify this as the NGCU described in section 4.1.

The two choices of zero boundary condition used here (at a point on the southeastern coast of Australia for the WBC calculation and along the coast of South America for the interior Rossby model) mean that the complete solution reflects the influence only of winds over the interior South Pacific. Note that the logic of the solution described above, with long Rossby waves propagating due west, our neglect of potential effects of waves emanating from the coast of South America, and the linear assumption that information travels only equatorward along the coast of Australia, means that equatorial winds play no role in the model solution. The principal advantage of this combined linear model is that it allows isolating its two distinct elements, the WBC carrying influences from the subtropics, and the jet from the southern tip of the Solomons carrying tropical influences over 5°S–11.5°S, that together form the net transport anomalies entering the Solomon Sea. Further, such a linear model allows studying these forcing elements in frequency bands (e.g., annual and interannual), or experimenting with effects of regional winds that can freely be isolated and added together to recover the complete solution.

References

Alberty, M.S., Sprintall, J., MacKinnon, J., Ganachaud, A., Cravatte, S., Eldin, G., Germineaud, C., Melet, A., 2017. Patterns of mixing in the Solomon Sea. J. Geophys. Res. Oceans 122, 4021–4039. doi:10.1002/2016JC012666.

Anutaliya, A., Send, U., Sprintall, J., McClean, J.L., Lankhorst, M., Koelling, J., 2019. Mooring and PIES end-point measurements at the southern entrance of the Solomon Sea: subseasonal to interannual flow variability. J. Geophys. Res. Submitted.

Atlas, R., Hoffman, R.N., Ardizzone, J., Leidner, S.M., Jusem, J.C., Smith, D.K., Gombos, D., 2011. A cross-calibrated, multiplatform ocean surface wind velocity product for meteorological and oceanographic applications. Bull. Amer. Meteor. Soc. 92, 157–174. doi:10.1175/2010BAMS2946.1.

Chen, S., Qiu, B., 2004. Seasonal variability of the South Equatorial Countercurrent. J. Geophys. Res. 109, C08003. doi:10.1029/2003JC002243.

Chen, Z., Wu, L., Qiu, B., Sun, S., Jia, F., 2014. Seasonal variation of the South Equatorial Current bifurcation off Madagascar. J. Phys. Oceanogr. 44, 618–631. doi:10.1175/JPO-D-13-0147.1.

Choukroun, S., Ridd, P.V., Brinkman, R., McKinna, L.I.W., 2010. On the surface circulation in the western Coral Sea and residence times in the Great Barrier Reef. J. Geophys. Res. 115, C06013. doi:10.1029/2009JC005761.

Couvelard, X., Marchesiello, P., Gourdeau, L., Lefebvre, J., 2008. Barotropic zonal jets induced by islands in the Southwest Pacific. J. Phys. Oceanogr. 38, 2185–2204. doi:10.1175/2008JPO3903.1.

Cravatte, S., Ganachaud, A., Duong, Q.P., Kessler, W.S., Eldin, G., Dutrieux, P., 2011. Observed circulation in the Solomon Sea from SADCP data. Prog. Oceanogr. 88, 116–130. doi:10.1016/j.pocean.2010.12.015.

Davis, R.E., 1976. Predictability of sea surface temperature and sea level pressure anomalies over the North Pacific Ocean. J. Phys. Oceanogr. 6, 249–266. doi:10.1175/1520-0485(1976)006<0249:possta>2.0.co;2.

Davis, R.E., 2005. Intermediate-depth circulation of the Indian and South Pacific Oceans measured by autonomous floats. J. Phys. Oceanogr. 35, 683–707. doi:10.1175/jpo2702.1.

Davis, R.E., 2016. Solomon Sea ocean transport from gliders [Data set]. Scripps Institution of Oceanography, Instrument Development Group doi:10.21238/s8SPRAY2718.

Davis, R.E., Kessler, W.S., Sherman, J.T., 2012. Gliders measure western boundary current transport from the South Pacific to the equator. J. Phys. Oceanogr. 42, 2001–2013. doi:10.1175/JPO-D-12-022.1.

England, M.H., McGregor, S., Spence, P., Meehl, G.A., Timmermann, A., Cai, W., Sen Gupta, A., McPhaden, M.J., Purich, A., Santoso, A., 2014. Recent intensification of wind-driven circulation in the Pacific and the ongoing warming hiatus. Nature Clim. Change 4, 222–227. doi:10.1038/nclimate2106.

Fernandez, D., Bowen, M., Carter, L., 2014. Intensification and variability of the confluence of subtropical and subantarctic boundary currents east of New Zealand. J. Geophys. Res. Oceans 119, 1146–1160. doi:10.1002/2013JC009153.

Fine, R.A., Lukas, R., Bingham, F.M., Warner, M.J., Gammon, R.H., 1994. The western equatorial Pacific: A water mass crossroads. J. Geophys. Res. 99, 25,063–25,080. doi:10.1029/94JC02277.

Firing, E., Qiu, B., Miao, W., 1999. Time-dependent island rule and its applications to the time-varying North Hawaiian Ridge Current. J. Phys. Oceanogr. 29, 2671–2688. doi:10.1175/1520-0485(1999)029<2671:TDIRAI>2.0.CO;2.

Fu, L., Qiu, B., 2002. Low-frequency variability of the North Pacific Ocean: The roles of boundary- and wind-driven baroclinic Rossby waves. J. Geophys. Res. 107, 3220. doi:10.1029/2001JC001131.

Ganachaud, A., Cravatte, S., Sprintall, J., Germineaud, C., Alberty, M., CoAuthors, 2017. The Solomon Sea: its circulation, chemistry, geochemistry and biology explored during two oceanographic cruises. Elem. Sci. Anth. 5. doi:10.1525/elementa.221.

Gasparin, F., Ganachaud, A., Maes, C., Marin, F., Eldin, G., 2012. Oceanic transports through the Solomon Sea: The bend of the New Guinea Coastal Undercurrent. Geophys. Res. Lett. 39, L15608. doi:10.1029/2012GL052575.

Germineaud, C., Ganachaud, A., Sprintall, J., Cravatte, S., Eldin, G., Alberty, M.S., Privat, E., 2016. Pathways and water mass properties of the thermocline and intermediate waters in the Solomon Sea. J. Phys. Oceanogr. 46, 3031–3049. doi:10.1175/JPO-D-16-0107.1.

Godfrey, J.S., 1975. On ocean spindown I: A linear experiment. J. Phys. Oceanogr. 5, 399–409.

Godfrey, J.S., 1989. A Sverdrup model of the depth-integrated flow for the world ocean allowing for island circulations. Geophys. Astrophys. Fluid Dyn. 45, 89–112. doi:10.1080/03091928908208894.

Goodman, P.J., Hazeleger, W., de Vries, P., Cane, M., 2005. Pathways into the Pacific Equatorial Undercurrent: A trajectory analysis. J. Phys. Oceanogr. 35, 2134–2151. doi:10.1175/JPO2825.1.

Gordon, A.L., Sprintall, J., Van Aken, H.M., Susanto, D., Wijffels, S., Molcard, R., Ffield, A., Pranowo, W., Wirasantosa, S., 2010. The Indonesian throughflow during 2004–2006 as observed by the INSTANT program. Dyn. Atmos. Oceans 50, 115–128. doi:10.1016/j.dynatmoce.2009.12.002.

Gourdeau, L., Kessler, W.S., Davis, R.E., Sherman, J., Maes, C., , Kestenare, E., 2008. Zonal jets entering the Coral Sea. J. Phys. Oceanogr. 38, 715–725. doi:10.1175/2007JPO3780.1.

Gourdeau, L., Verron, J., Chaigneau, A., Cravatte, S., Kessler, W., 2017. Complementary use of glider data, altimetry, and model for exploring mesoscale eddies in the tropical Pacific Solomon Sea. J. Geophys. Res. Oceans 122, 9209–9229. doi:10.1002/2017JC013116.

Grenier, M., Cravatte, S., Blanke, B., Menkes, C., Koch-Larrouy, A., Durand, F., Melet, A., Jeandel, C., 2011. From the western boundary currents to the Pacific Equatorial Undercurrent: Modeled pathways and water mass evolutions. J. Geophys. Res. 116, C12044. doi:10.1029/2011JC007477.

Horel, J.D., 1984. Complex principal component analysis: Theory and examples. J. Climate Appl. Meteor. 23, 1660–1673. doi:10.1175/1520-0450(1984)023<1660:CPCATA>2.0.CO;2.

Hristova, H.G., Kessler, W.S., 2012. Surface circulation in the Solomon Sea derived from Lagrangian drifter observations. J. Phys. Oceanogr. 42, 448–458. doi:10.1175/JPO-D-11-099.1.

Ishida, A., Kashino, Y., Hosoda, S., Ando, K., 2008. North-south asymmetry of warm water volume transport related with El Niño variability. Geophys. Res. Lett. 35, L18612. doi:10.1029/2008GL034858.

Iudicone, D., Rodgers, K.B., Schopp, R., Madec, G., 2007. An exchange window for the injection of Antarctic Intermediate Water into the South Pacific. J. Phys. Oceanogr. 37, 31–49. doi:10.1175/JPO2985.1.

Izumo, T., 2005. The equatorial undercurrent, meridional overturning circulation, and their roles in mass and heat exchanges during El Niño events in the tropical Pacific ocean. Ocean Dyn. 55, 110–123. doi:10.1007/S10236-005-0115-1.

Izumo, T., Picaut, J., Blanke, B., 2002. Tropical pathways, equatorial undercurrent variability and the 1998 La Niña. Geophys. Res. Lett. 29, 2080. doi:10.1029/2002GL015073.

Jin, F.F., 1997. An equatorial ocean recharge paradigm for ENSO. Part I: Conceptual model. J. Atmos. Sci. 54, 811–829. doi:10.1175/1520-0469(1997)054<0811:AEORPF>2.0.CO;2.

Kessler, W.S., 1990. Observations of long Rossby waves in the northern tropical Pacific. J. Geophys. Res. 95, 5183–5217. doi:10.1029/JC095iC04p05183.

Kessler, W.S., 2002. Is ENSO a cycle or a series of events? Geophys. Res. Lett. 29, 2125. doi:10.1029/2002GL015924.

Kessler, W.S., Cravatte, S., 2013a. ENSO and short-term variability of the South Equatorial Current entering the Coral Sea. J. Phys. Oceanogr. 43, 956–969. doi:10.1175/JPO-D-12-0113.1.

Kessler, W.S., Cravatte, S., 2013b. Mean circulation of the Coral Sea. J. Geophys. Res. Oceans 118, 6385–6410. doi:10.1002/2013JC009117.

Kessler, W.S., McCreary, J.P., 1993. The annual wind-driven Rossby wave in the subthermocline equatorial Pacific. J. Phys. Oceanogr. 23, 1192–1207. doi:10.1175/1520-0485(1993)023<1192:TAWDRW>2.0.CO;2.

Kug, J.S., Kang, I.S., An, S.I., 2003. Symmetric and antisymmetric mass exchanges between the equatorial and off-equatorial Pacific associated with ENSO. J. Geophys. Res. 108, 3284. doi:10.1029/2002JC001671.

Lee, T., Fukumori, I., 2003. Interannual-to-decadal variations of Tropical-Subtropical exchange in the Pacific Ocean: Boundary versus interior pycnocline transports. J. Clim. 16, 4022–4042. doi:10.1175/1520-0442(2003)016<4022:IVOTEI>2.0.CO;2.

Lee, T., Fukumori, I., Menemenlis, D., Xing, Z., Fu, L.L., 2002. Effects of the Indonesian throughflow on the Pacific and Indian Oceans. J. Phys. Oceanogr. 32, 1404–1429. doi:10.1175/1520-0485(2002)032<1404:EOTITO>2.0.CO;2.

Lee, T., Fukumori, I., Tang, B., 2004. Temperature advection: Internal versus external processes. J. Phys. Oceanogr. 34, 1936–1944. doi:10.1175/1520-0485(2004)034<1936:TAIVEP>2.0.CO;2.

L'Heureux, M.L., Lee, S., Lyon, B., 2013. Recent multidecadal strengthening of the Walker circulation across the tropical Pacific. Nature Clim. Change 3, 571–576. doi:10.1038/nclimate1840.

Lindstrom, E., Lukas, R., Fine, R., Firing, E., Godfrey, S., Meyers, G., Tsuchiya, M., 1987. The Western Equatorial Pacific Ocean Circulation Study. Nature 330, 533–537. doi:10.1038/330533a0.

Mata, M.M., Tomczak, M., Wijffels, S., Church, J.A., 2000. East Australian Current volume transports at 30°S: Estimates from the World Ocean Circulation Experiment hydrographic sections PR11/P6 and the PCM3 current meter array. J. Geophys. Res. 105, 28,509–28,526. doi:10.1029/1999JC000121.

McCartney, M.S., 1982. The subtropical recirculation of Mode Waters. J. Mar. Res. 40 Supplement, 427–464.

McPhaden, M.J., Timmermann, A., Widlansky, M.J., Balmaseda, M.A., Stockdale, T.N., 2015. The curious case of the El Niño that never happened: A perspective from 40 years of progress in climate research and forecasting. Bull. Amer. Meteorol. Soc. 96, 1647–1665. doi:10.1175/BAMS-D-14-00089.1.

Meinen, C.S., McPhaden, M.J., 2000. Observations of warm water volume changes in the equatorial Pacific and their relationship to El Niño and La Niña. J. Clim. 13, 3551–3559. doi:10.1175/1520-0442(2000)013<3551:OOWWVC>2.0.CO;2.

Melet, A., Gourdeau, L., Verron, J., 2010. Variability in Solomon Sea circulation derived from altimeter sea level data. Ocean Dyn. 60, 883–900. doi:10.1007/s10236-010-0302-6.

Meyers, G., 1979. On the annual Rossby wave in the tropical North Pacific Ocean. J. Phys. Oceanogr. 9, 663–674. doi:10.1175/1520-0485(1979)009<0663:OTARWI>2.0.CO;2.

Minobe, S., Takeuchi, K., 1995. Annual period Rossby waves in the Pacific Ocean. J. Geophys. Res. 100, 18,379–18,392. doi:10.1029/95JC01666.

Pena, L.D., Goldstein, S.L., Hemming, S.R., Jones, K.M., Calvo, E., Pelejero, C., Cacho, I., 2013. Rapid changes in meridional advection of Southern Ocean intermediate waters to the tropical Pacific during the last 30 kyr. Earth Plan. Sci. Lett. 368, 20–32. doi:10.1016/j.epsl.2013.02.028.

Qin, X., Sen Gupta, A., van Sebille, E., 2015. Variability in the origins and pathways of Pacific Equatorial Undercurrent water. J. Geophys. Res. Oceans 120, 3113–3128. doi:10.1002/2014JC010549.

Qiu, B., Chen, S., Kessler, W.S., 2009. Source of the 70-day mesoscale eddy variability in the Coral Sea and North Fiji Basin. J. Phys. Oceanogr. 39, 404–420. doi:10.1175/2008JPO3988.1.

Qiu, B., Mai, M., Kashino, Y., 1999. Intraseasonal variability in the Indo-Pacific Throughflow and the regions surrounding the Indonesian Seas. J. Phys. Oceanogr. 29, 1599–1618. doi:10.1175/1520-0485(1999)029<1599:IVITIP>2.0.CO;2.

Qu, T., Lindstrom, E.J., 2002. A climatological interpretation of the circulation in the western South Pacific. J. Phys. Oceanogr. 32, 2492–2508. doi:10.1175/1520-0485(2002)032<2492:ACIOTC>2.0.CO;2.

Ridgway, K.R., Dunn, J.R., 2003. Mesoscale structure of the mean East Australian Current System and its relationship with topography. Progr. Oceanogr. 56, 189–222. doi:10.1016/S0079-6611(03)00004-1.

Ridgway, K.R., Dunn, J.R., 2007. Observational evidence for a Southern Hemisphere oceanic supergyre. Geophys. Res. Lett. 34, L13612. doi:10.1029/2007GL030392.

Ridgway, K.R., Godfrey, J.S., 1997. Seasonal cycle of the East Australian Current. J. Geophys. Res. 102, 22,921–22,936. doi:10.1029/97JC00227.

Roemmich, D., Gilson, J., 2009. The 2004–2008 mean and annual cycle of temperature, salinity, and steric height in the global ocean from the Argo Program. Progr. Oceanogr. 82, 81–100. doi:10.1016/j.pocean.2009.03.004.

Roemmich, D., Woodworth, P., Jevrejeva, S., Purkey, S., Lankhorst, M., Send, U., Maximenko, N., 2017. In situ observations needed to complement, validate, and interpret satellite altimetry, in: Stammer, D., Cazenave, A. (Eds.), Satellite Altimetry over Oceans and Land Surfaces. CRC Press, pp. 113–148. ISBN 9781498743457.

Rudnick, D.L., Cole, S.T., 2011. On sampling the ocean using underwater gliders. J. Geophys. Res. 116, C08010. doi:10.1029/2010JC006849.

Rudnick, D.L., Davis, R.E., Sherman, J.T., 2016. Spray underwater glider operations. J. Atmos. Oceanic Technol. 33, 1113–1122. doi:10.1175/JTECH-D-15-0252.1.

Schonau, M.C., Rudnick, D.L., 2017. Mindanao Current and Undercurrent: Thermohaline structure and transport from repeat glider observations. J. Phys. Oceanogr. 47, 2055–2075. doi:10.1175/JPO-D-16-0274.1.

Scully-Power, P.D., 1973. Coral Sea flow budgets in winter. Aust. J. Mar. Freshw. Res. 24, 203–216. doi:10.1071/MF9730203.

Sherman, J., Davis, R.E., Owens, W.B., Valdes, J., 2001. The autonomous underwater glider "Spray". IEEE J. Oceanic Eng. 26, 437–446. doi:10.1109/48.972076.

Sokolov, S., Rintoul, S., 2000. Circulation and water masses of the southwest Pacific: WOCE section P11, Papua New Guinea to Tasmania. J. Mar. Res. 58, 223–268. doi:10.1357/002224000321511151.

Sprintall, J., Révelard, A., 2014. The Indonesian throughflow response to Indo-Pacific climate variability. J. Geophys. Res. Oceans 119, 1161–1175. doi:10.1002/2013JC009533.

Sprintall, J., Wijffels, S.E., Molcard, R., Jaya, I., 2009. Direct estimates of the Indonesian throughflow entering the Indian Ocean: 2004–2006. J. Geophys. Res. 114, C07001. doi:10.1029/2008JC005257.

Srinivasan, K., McWilliams, J.C., Renault, L., Hristova, H.G., Molemaker, J., Kessler, W.S., 2017. Topographic and mixed-layer submesoscale currents in the near-surface southwestern tropical Pacific. J. Phys. Oceanogr. 47, 1221–1242. doi:10.1175/JPO-D-16-0216.1.

Sverdrup, H.U., 1947. Wind-driven currents in a baroclinic ocean; with application to the equatorial currents of the eastern Pacific. Proceedings of the National Academy of Sciences USA 33, 318–326.

Toggweiler, J.R., Dixon, K., Broecker, W.S., 1991. The Peru upwelling and the ventilation of the south Pacific thermocline. J. Geophys. Res. 96, 20,467–20,497. doi:10.1029/91JC02063.

Tsuchiya, M., 1981. The origin of the Pacific equatorial 13°C water. J. Phys. Oceanogr. 11, 794–812. doi:10.1175/1520-0485(1981)011<0794:TOOTPE>2.0.CO;2.

Tsuchiya, M., Lukas, R., Fine, R.A., Firing, E., Lindstrom, E., 1989. Source waters of the Pacific Equatorial Undercurrent. Progr. Oceanogr. 23, 101–147. doi:10.1016/0079-6611(89)90012-8.

Vega, A., du Penhoat, Y., Dewitte, B., Pizarro, O., 2003. Equatorial forcing of interannual Rossby waves in the eastern South Pacific. Geophys. Res. Lett. 30, 1197. doi:10.1029/2002GL015886.

Wajsowicz, R.C., 1993. The circulation of the depth-integrated flow around an island with application to the Indonesian Throughflow. J. Phys. Oceanogr. 23, 1470–1484. doi:10.1175/1520-0485(1993)023<1470:TCOTDI>2.0.CO;2.

Xue, Y., Wen, C., Kumar, A., Balmaseda, M., Fujii, Y., Alves, O., Martin, M., Yang, X., Vernieres, G., Desportes, C., Lee, T., Ascione, I., Gudgel, R., Ishikawa, I., 2017. A real-time ocean reanalyses intercomparison project in the context of tropical Pacific observing system and ENSO monitoring. Clim. Dyn. 11–12, 3647–3672. doi:10.1007/s00382-017-3535-y.

Yamagami, Y., Tozuka, T., 2015. Interannual variability of South Equatorial Current bifurcation and western boundary currents along the Madagascar coast. J. Geophys. Res. Oceans 120, 8551–8570. doi:10.1002/2015JC011069.